Master's thesis
Master's programme in Atmospheric sciences
Meteorology

Model-simulated present-day distributions and projected future changes in top-of-the-atmosphere radiation fluxes and surface energy budget

Anni Kröger

28.11.2019

Supervisor: Jouni Räisänen

Reviewers: Jouni Räisänen, Heikki Järvinen

University of Helsinki
Faculty of Science
P.O. Box 64 (Gustaf Hällströmin katu 2)
00014 University of Helsinki

Contents

HELSINGIN YLIOPISTO
HELSINGFORS UNIVERSITET
UNIVERSITY OF HELSINKI
MATEMAATTIS-LUONNONTIETEELLINEN TIEDEKUNTA
MATEMATISK-NATURVETENSKAPLIGA FAKULTETEN
FACULTY OF SCIENCE

Tiedekunta – Fakultet – Faculty	Koulutusohjelma – Utbildningsprogram – Degree programme	
Faculty of Science	Master's Programme in Atmospheric Sciences/Meteorology	
Tekijä – Författare – Author		
Anni Kröger		
Työn nimi – Arbetets titel – Title		
Model-simulated present-day distributions and projected future changes in top-of-the-atmosphere radiation fluxes and surface energy budget		
Työn laji – Arbetets art – Level	Aika – Datum – Month and year	Sivumäärä – Sidoantal – Number of pages
Master's thesis	November 2019	51 p.

Tiivistelmä – Referat – Abstract

Earth's energy budget describes the balance between the net incoming and outgoing energy fluxes, and the energy balance approach can be used to better understand the basic physical mechanisms of climate change. Anthropogenic changes in the atmospheric composition, such as increases in greenhouse gases, drive changes in climate system which in turn can cause rising of the global temperatures. Various feedbacks, associated with increase in atmospheric water vapor content, changes in clouds and reduced snow/ice cover, affect the pattern of surface warming by altering the fluxes of energy. By studying the energy balance at the top of the atmosphere and at the surface, we gain useful information about the climate system's response to changes in the atmospheric composition.

In this thesis, data for 23 climate models in the fifth phase of the Coupled Model Intercomparison Project (CMIP5) was used. The present-day distributions and future projections of the simulated changes (under RCP8.5 emission scenario, Representative Concentration Pathway) for 14 radiative and non-radiative energy budget components, along with the changes in surface temperature and cloud cover were studied, with baseline period of 1981-2010 and a comparison scenario period of 2071-2100. The geographical distributions of the multimodel mean changes and their global averages were analysed. Additionally, the intermodel consistency of the simulated changes was studied with the intermodel standard deviations and the ratio of multimodel mean change to the intermodel standard deviation. Furthermore, the intermodel correlation between the change in surface temperature and each energy budget variable was discussed.

A general finding was that the multimodel mean surface temperature increases everywhere, more over land than oceans, and that the warming is amplified over the northern polar regions. The changes were largest for the thermal radiation fluxes, and the dominating contribution to the surface warming was concluded to be the change in clear-sky atmospheric re-radiation component. However, increase in absorbed shortwave radiation, presumably due to reduced ice/snow cover and increase in atmospheric water vapor content, was also found to be substantial, and there was a strong negative correlation between the clear-sky downward shortwave radiation flux and the change in temperature over the low-to-mid latitudes. The comparison of contribution of the changes in longwave and shortwave fluxes to global warming in the near-future and long-term climate model projections could be an interesting subject for future studies. Additionally, the changes in the surface energy fluxes were found to modify the pattern of surface warming.

Avainsanat – Nyckelord – Keywords
Temperature change, energy balance, surface energy budget, CMIP5

Säilytyspaikka – Förvaringställe – Where deposited

Muita tietoja – Övriga uppgifter – Additional information

HELSINGIN YLIOPISTO
HELSINGFORS UNIVERSITET
UNIVERSITY OF HELSINKI

MATEMAATTIS-LUONNONTIETEELLINEN TIEDEKUNTA
MATEMATISK-NATURVETENSKAPLIGA FAKULTETEN
FACULTY OF SCIENCE

Tiedekunta – Fakultet – Faculty	Koulutusohjelma – Utbildningsprogram – Degree programme	
Matemaattis-luonnontieteellinen	Ilmakehätieteiden maisteriohjelma/Meteorologia	
Tekijä – Författare – Author		
Anni Kröger		
Työn nimi – Arbetets titel – Title		
Model-simulated present-day distributions and projected future changes in top-of-the-atmosphere radiation fluxes and surface energy budget		
Työn laji – Arbetets art – Level	Aika – Datum – Month and year	Sivumäärä – Sidoantal – Number of pages
Pro gradu -tutkielma	Marraskuu 2019	51 s.

Tiivistelmä – Referat – Abstract

Maapallon energiatalous kuvaa eri energiavoiden kulkua ilmastojärjestelmässä (maanpinta ja ilmakehä) ja säteilytasapainoa ilmakehän ulkorajalla. Tarkastelemalla Maan energiatalouden toteutumistapaa voidaan tuottaa hyödyllistä tietoa ilmastonmuutoksesta ja ymmärtää paremmin ilmastonvaihteluiden fysikaalisia mekanismeja. Ihmisten toiminnasta syntyvä kasvihuonekaasujen pitoisuuksien kasvu ilmakehässä aiheuttaa muutoksia ilmastojärjestelmään, joiden seurauksena ilmasto lämpenee. Maanpinnalla lämpötilajakauman muutoksiin vaikuttavat lisäksi lukuisat eri palauteilmiöt, jotka voivat vahvistaa tai heikentää alkuperäisiä muutoksia Maan energiatasapainossa. Esimerkkejä tärkeistä palauteilmiöistä ovat vesihöyryn kasvihuoneilmiö, lumi- ja jääpeitteen sekä pilvisyyden muutokset. Tutkimalla energiatalouden toteutumista ilmakehän ulkorajalla sekä maanpinnalla saadaan käsitys siitä, miten ilmastojärjestelmä reagoi muutoksiin ilmakehän koostumuksessa.

Tässä työssä käytettiin 23 ilmastomallin tuloksia, jotka saatiin hankkeesta CMIP5 (Coupled Model Intercomparison Project Phase 5). Simulaatioiden tulosten avulla tutkittiin 14 energiatalouden komponentin, pintalämpötilan ja kokonaispilvisyyden jakaumia nykypäivän ilmasto-oloissa (perusjakso 1981-2010) sekä niiden muutoksia vertailujaksolla 2071-2100 RCP8.5-päästöskenaarion (Representative Concentration Pathway) mukaan. Tulokset esitettiin 23 mallin keskiarvona, ja tutkielmassa analysoitiin muutosten maantieteellisiä jakaumia sekä komponenttien keskimääräistä muutosta maapallolla. Ilmastomallien simuloimien tulosten yhteneväisyyttä tutkittiin mallienvälisen keskihajonnan avulla, sekä tarkastelemalla kaikkien mallien keskimääräisen muutoksen ja mallienvälisen hajonnan suhdetta. Lisäksi pintalämpötilan ja energiatalouskomponenttien muutosten välistä yhteyttä tutkittiin tarkastelemalla niiden mallienvälistä korrelaatiota.

Ilmastomallien mukaan Maan pintalämpötila nousee kaikkialla, lämpötila kasvaa enemmän maa- kuin merialueilla, ja lämpeneminen on voimakkainta pohjoisilla korkeilla leveysasteilla. Lämpösäteilyvoiden muutokset olivat suurimpia, ja pintalämpötilan nousuun vaikutti eniten muutos ilmakehän vastasäteilyssä (pilvettömissä olosuhteissa). Absorboituneen lyhytaaltosäteilyn määrän lisääntyminen oli myös merkittävä, mikä todennäköisesti oli seurausta lumi- ja jääpeitteen vähenemisestä sekä ilmakehän vesihöyrysisällön kasvusta, ja pintaa kohti suuntautuvan lyhytaaltosäteilyn muutoksen (pilvettömissä olosuhteissa) ja pintalämpötilan muutoksen välillä oli vahva negatiivinen korrelaatio. Lyhyt- ja pitkäaaltosäteilyvoiden muutosten vaikutusten keskinäinen vertailu suhteessa ilmaston lämpenemiseen olisi kiinnostava aihe tämän tutkielman jatkoksi. Lisäksi todettiin, että pinnan energiavoiden muutokset muokkaavat pintalämpötilan muutoksen jakaumaa.

Avainsanat – Nyckelord – Keywords

Ilmaston lämpeneminen, Maan energiatalous, pinnan lämpötalous, CMIP5

Säilytyspaikka – Förvaringställe – Where deposited

Muita tietoja – Övriga uppgifter – Additional information

1 Introduction

Several studies (see for instance [Collins et al., 2013, Räisänen, 2016]) of Earth's current and model simulated future climate suggest that human activities and consequent increases in the atmospheric greenhouse gases increase the top-of-the-atmosphere energy imbalance, causing global warming. From the perspective of Earth's energy budget, alterations in the energy fluxes at the top of the atmosphere drive changes in the climate system, and the resulting changes in the components of the surface energy budget modify and contribute to the pattern of surface warming. Various feedbacks, related to for example changes in atmospheric water vapor content, ice/snow cover or cloudiness, alter the fluxes of energy.

The purpose of this study is to use the energy balance approach to better understand the basic physical mechanisms of climate change, and to gain useful information about the climate system's simulated response to increases in greenhouse gas emissions and concentrations. We study how the changes in the top-of-the-atmosphere radiation balance and the surface energy budget are related to the near-surface air temperature change, and we discuss whether they are related directly and/or through feedback mechanisms. By studying the changes in the components of the surface energy budget, in addition to the top-of-the-atmosphere radiation fluxes, we can get valuable information on the climate model simulated changes in surface climate and in the lower atmospheric layers.

In this thesis, we analyse the climate model simulated future global and annual mean changes in the top-of-the-atmosphere radiation balance and the surface energy budget, along with the change in near-surface air temperature and cloud cover. We use data for 23 models in the fifth phase of the Coupled Model Intercomparison Project [Taylor et al., 2011] and study the multimodel means for each variable with two averaging periods: a baseline period of 1981-2010 for the simulated current climate, and a comparison scenario period (RCP8.5, *Representative Concentration Pathway*) of 2071-2100 for the future projections. For the results, global averages and geographical distributions are presented, and physical interpretations of the distributions are discussed.

Uncertainty in climate simulations is due to various factors, including internal variability in the climate system, scenario assumptions and choices of modelling techniques [Collins et al., 2013]. In addition to the multimodel mean projections, confidence in results is analysed with the intermodel differences in changes and the model-to-model agreement of the sign and magnitude of the projections. The intermodel correlation between the change in surface temperature and each energy budget variable (or cloud cover) is studied to see, for instance, whether or not

models with larger warming also project stronger positive or negative change in other variables.

We expect that the mean surface temperature will rise in each simulation and that, according to the Clasius-Clapeyron relation, the atmospheric water vapor content increases due to the projected warming. The thermal radiation from the surface is expected to increase, since it is directly proportional to the fourth power of the surface temperature. The enhanced greenhouse effect and increases in atmospheric greenhouse gases, such as water vapor, make the atmosphere less transparent to longwave radiation and stronger absorption and emissions of thermal radiation occur, thereby increasing the atmospheric re-radiation and adding to the initial warming of the surface. Therefore, we hypothesise that the projected changes in the downward thermal radiation fluxes are largest and that the dominating contribution to the eventual warming is increases in the clear-sky atmospheric re-radiation. However, most of the re-radiation occurs from the lower atmospheric layers where the temperature change is close to the pattern of surface warming [Zhao et al., 1994], therefore partly explaining the expected strong correlation between the clear-sky atmospheric re-radiation component and the change in surface temperature. Furthermore, we expect there to be notable geographical variations in the distributions of the surface energy fluxes and the temperature change, for example land-ocean contrasts. Therefore, in addition to the thermal radiation fluxes, other components of the energy balance are expected to modify the pattern of surface warming to some extent.

The energy budget perspective on Earth's climate system and a few key concepts in climate science are described in Chapter 2. A more detailed description of the data and methods used in this thesis is presented in Chapter 3. The results are discussed in Chapters 4, 5 and 6, starting from the simulated present-day distributions of the studied variables, then proceeding to the projected future changes, and lastly the intermodel consistency of the simulated changes is examined. The main conclusions and suggestions for further studies are presented in Chapter 7.

2 Energy budget perspective on Earth's climate

This chapter presents a few key concepts in climate science from the energy budget perspective. First, Earth's global mean energy budget is studied and its components are introduced. Then, a brief overview of the greenhouse effect and climate forcing is given. Lastly, the climate sensitivity and climate feedbacks are described shortly. Altogether, this chapter will provide an understanding of the basics of these phenomena, which will be needed throughout this thesis.

2.1 Global mean energy budget

Earth's energy budget describes the balance between the net incoming and outgoing energy flows. For a steady climate, the incident solar radiation at the top of the atmosphere is balanced by the reflected solar radiation and the emitted thermal radiation. Figure 1 shows a diagram of present-day Earth's global and annual mean energy budget. The unit used for measuring the energy fluxes is watt per square meter (W/m^2).

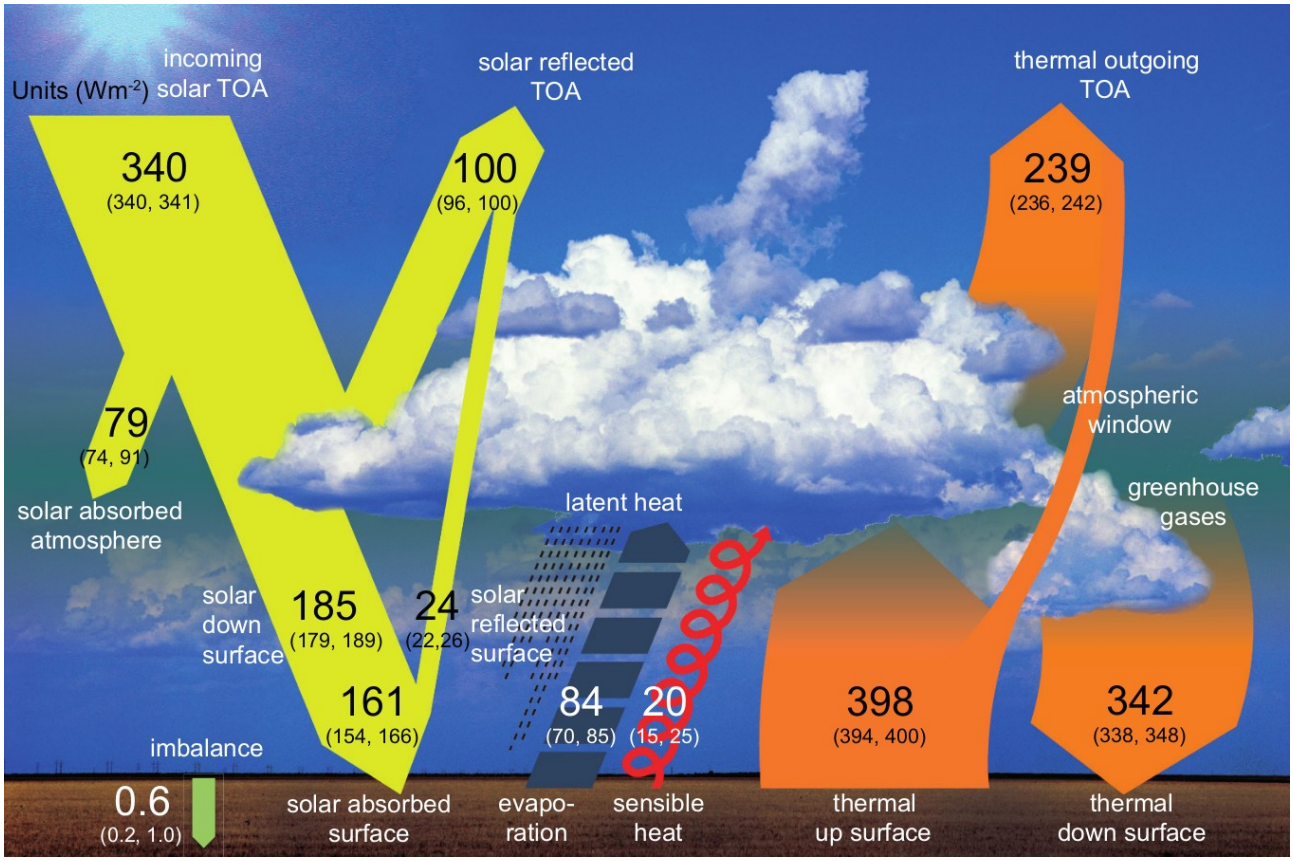

Figure 1: Present-day Earth's globally and annually averaged energy budget [Hartmann et al., 2013] (adapted from [Wild et al., 2013]). The numbers correspond to the magnitudes of the energy budget components and their uncertainty ranges, units W/m^2.

At the top of the atmosphere (TOA), the average incoming solar radiation is, according to the current estimate, 340 W/m^2 (Fig. 1). Part of this shortwave radiation (SW) is reflected back to space and the estimated total reflection is 100 W/m^2. Most of the reflection occurs in the atmosphere due to clouds, gas molecules and aerosols (76 W/m^2), and the rest from the surface (24 W/m^2). The outgoing longwave radiation (OLR) is thermal radiation emitted from the atmosphere and the surface. The average magnitude of the OLR flux is about 239 W/m^2. Hence, there is a slight imbalance in the TOA radiation budget due to the present-day climate change, approximately 0.6 W/m^2 [Hansen et al., 2011].

In the atmosphere, clouds, aerosols, water vapor and the ozone layer absorb part of the downwelling SW radiation (79 W/m^2). The solar radiation absorbed at the surface is approximately 161 W/m^2, while the average emitted longwave (LW) radiation from the surface is 398 W/m^2. The atmosphere is partly opaque to LW radiation, therefore absorbing a large part of the upwelling thermal radiation. In the atmosphere, LW radiation is emitted to space and towards the surface, the latter defined as the atmospheric re-radiation. The downwelling LW radiation from the atmosphere (approximately 342 W/m^2) compensates about 85 % of the energy loss due to the surface emitted LW radiation.

When viewed separately, there is a negative net flux of radiation energy in the atmosphere (-104 W/m^2) and approximately equal but positive flux on the surface (105 W/m^2). This is balanced by sensible heat flux (20 W/m^2) and latent heat flux (84 W/m^2). On average, both transfer heat from the surface to the atmosphere. A more detailed explanation of the mechanisms of the turbulent heat fluxes can be found in Chapter 4.3.2.

The surface energy budget and the TOA radiation balance are both studied in this thesis. The components of the TOA radiation budget can be observed and the data is gathered by satellites. The magnitudes of the surface energy fluxes have more uncertainty since direct satellite measurements can not be made similarly [Wild et al., 2013]. Nevertheless, the values presented in Figure 1 are good estimates. As mentioned earlier, it is important to note that here the magnitudes of the components are global and annual averages. In reality, the fluxes vary depending on, for example, the location and the time of the year.

Current observations suggest the Earth is not in energy balance and that the global mean surface air temperature has increased in recent decades [Cubasch et al., 2013]. In addition to natural forcings, human activities affect Earth's energy budget by generating the imbalance that drives changes in climate. The subsequent sections introduce a few key concepts related to this process.

2.2 The greenhouse effect and climate forcings

According to Figure 1, the current estimate for thermal radiation emitted from the surface is 398 W/m^2, but the downward atmospheric re-radiation is about 342 W/m^2. Thus, the average net energy loss from the surface due to LW radiation is approximately 56 W/m^2. While some of the atmospheric gases, such as oxygen, are virtually transparent to LW radiation, the greenhouse gases (GHGs) absorb and emit thermal radiation making the atmosphere partly opaque to LW radiation. Some of the most important GHGs in the atmosphere are water vapor, carbon dioxide

and methane, to name a few [Kiehl and Trenberth, 1997]. If the atmosphere was completely transparent to LW radiation, Earth's surface would be much cooler. The greenhouse effect describes the process where atmospheric absorption and emissions of LW radiation result in warming of the surface.

Changes in the atmospheric composition affect Earth's energy budget. For instance, increases in the concentrations of human-made GHGs strengthen the greenhouse effect by making the atmosphere more opaque to thermal radiation [Neelin, 2011]. At the top of the atmosphere, less LW radiation is emitted to space and the energy imbalance is increased. This results in rising surface temperatures until new energy balance is reached.

As an example of a human-induced *climate forcing*, the doubling of the CO_2 concentration in the atmosphere would reduce the TOA ougoing LW radiation by about 3.7 W/m^2 [Räisänen, 2014]. Neelin defines the term forcing as "an external cause driving a response in a system" [Neelin, 2011], where 'system' now refers to Earth, 'response' is a change in the TOA radiation balance and consequent changes in climate, while 'external cause' can be changes in the incident solar radiation or increase in atmospheric aerosols by volcanic eruptions, for instance [Hansen et al., 2011]. In addition to natural forcings, *anthropogenic* (human-made) forcings have mainly to do with altering the atmospheric composition by emissions. Radiative forcing, a change in the TOA net radiation, leads to feedbacks that can either amplify or diminish its effects.

2.3 Climate sensitivity and climate feedbacks

As previously mentioned, Earth's surface temperature changes in response to a forcing until new energy balance is achieved. *Climate sensitivity* is defined as the average change in the surface temperature per said forcing [Hansen et al., 2011]. The eventual temperature change depends on *climate feedbacks*, processes that can either increase or decrease the initial response to the forcing by altering the fluxes of energy described in section 2.1. The most important feedbacks are the water vapor feedback, snow and ice feedback and cloud feedback [Neelin, 2011].

The atmosphere can hold more water vapor as the global mean temperature rises, according to the Clausius-Clapeyron equation. Water vapor is a strong greenhouse gas, and an increase in atmospheric water vapor content therefore results in additional warming. Due to the water vapor feedback, less thermal radiation is emitted to space at the top of the atmosphere. Since it amplifies the initial climate response (warming), it is a positive feedback.

The snow/ice feedback is also a positive feedback that is larger in the higher latitudes.

Warming reduces the snow and ice cover, which have a high reflectivity compared to other types of surface. Therefore, less SW radiation is reflected from the surface and consequently more is absorbed by it, which adds again to the initial warming.

The cloud feedback is related to changes in the cloud cover. On one hand, clouds reflect incoming solar radiation, and on the other hand, less thermal radiation is emitted to space due to clouds. The net effect of clouds is studied more closely in Chapter 4.2.

In addition to the main fast feedbacks briefly discussed above, there are several other feedbacks that have not been mentioned here. For instance, an example of a slow feedback is the changes in the continental ice-sheet cover [Hansen et al., 2011]. In general, climate feedbacks modify the changes in climate by affecting Earth's energy budget. They also introduce more uncertainty in the estimation of the changes in climate modeling [Neelin, 2011]. To summarize the content of this chapter:

- Earth's energy budget describes the balance between the energy flux components.
- Earth's energy imbalance, caused by some external factor, defines a forcing.
- A forcing drives changes in climate that lead to climate feedbacks.
- Feedbacks amplify or diminish the initial climate response.
- The changes continue until new energy balance is reached.

3 Data and methods

This chapter describes the data and methods used in this thesis. The first two sections introduce the climate model data and the experiments studied, while the final section gives information on data processing and output. The output results and interpretations are presented in Chapters 4, 5 and 6.

3.1 CMIP5 Models

In this thesis, data for 23 coupled atmosphere-ocean global climate and Earth system models in the fifth phase of the Coupled Model Intercomparison Project (CMIP5, [Taylor et al., 2011]) were used. The models and some of their properties are listed in Table 1. From the long-term experiments, a historical run (1850-2005) and one future-projection simulation (RCP8.5, 2006-2300) were chosen to be studied. The historical run is forced by observed changes in the

atmospheric composition [Taylor et al., 2011]. The specifics of the latter experiment are defined in the subsequent section.

Model	Atmospheric grid [°]		Ocean grid [°]		No. vert. levels
	Latitude	Longitude	Latitude	Longitude	in atmosphere
ACCESS1.0	1.25	1.88	x	x	38
ACCESS1.3	1.25	1.88	x	x	38
CanESM2	2.79	2.81	0.93, 1.14	1.41	35
CNRM-CM5	1.4	1.41	x	x	31
CSIRO-Mk3.6.0	1.87	1.88	0.93, 0.95	1.88	18
GISS-E2-H	2	2.5	1	1	40
GISS-E2-H-CC	2	2.5	1	1	40
GISS-E2-R	2	2.5	1	1.25	40
GISS-E2-R-CC	2	2.5	1	1.25	40
HadGEM2-CC	1.25	1.88	0.34, 1	1	60
HadGEM2-ES	1.25	1.88	0.34, 1	1	38
inmcm4	1.5	2	0.5	1	21
IPSL-CM5A-LR	1.89	3.75	x	x	39
IPSL-CM5A-MR	1.27	2.5	x	x	39
IPSL-CM5B-LR	1.89	3.75	x	x	39
MIROC5	1.4	1.41	0.5, 0.5	1.41	40
MIROC-ESM	2.79	2.81	0.56, 1.71	1.41	80
MIROC-ESM-CHEM	2.79	2.81	0.56, 1.71	1.41	80
MPI-ESM-LR	1.87	1.88	x	x	47
MPI-ESM-MR	1.87	1.88	x	x	95
MRI-CGCM3	1.12	1.13	0.5, 0.5	1	48
NorESM1-M	1.89	2.5	x	x	26
NorESM1-ME	1.89	2.5	x	x	26

Table 1: List of CMIP5 models studied in this thesis and rounded values of their atmospheric and ocean grid resolutions (x denotes that the resolution cannot be read out) [ENES, 2019b]. If the resolution is not constant, two values are given (for the equator and the poles, respectively). Last column: number of vertical levels in the atmosphere [Flato et al., 2013].

3.2 The Representative Concentration Pathways

The evolution of greenhouse gas emissions and concentrations and changes in other forcing agents are important elements in climate research. Various emission scenarios have been developed to be used as input for climate model simulations [Räisänen, 2014]. The Representative Concentration Pathways (RCPs) are a set of scenarios named after the estimated target level radiative forcing of year 2100: RCP2.6, RCP4.5, RCP6 and RCP8.5 [van Vuuren et al., 2011]. With help of integrated assessment models it is possible to describe, for instance, the socio-economic and technological changes or *pathways* that lead to these levels of the radiative forcing at the end of the century [Räisänen, 2014].

In this thesis, the RCP8.5 scenario is studied. RCP8.5 is a high emission scenario since the level of forcing is the highest of the four scenarios (8.5 W/m^2) and it has the highest greenhouse gas emissions and concentration levels compared to the other RCPs (1370 ppm CO_2 equivalent in 2100 [ENES, 2019a]). According to the scenario, the population growth will reach 12 billion by the end of the century, the energy technological development is slow and hence the burning of the fossil fuels is the primary source of energy [Riahi et al., 2011].

RCP8.5 might not be the most probable scenario of the RCPs in terms of future climate changes but it has some advantages over the other RCPs. Due to the strong forcing, the forced climate changes are large and therefore more clearly discernible from internal variability in the model simulations.

3.3 Data processing

The processing of the model data (Table 1) was performed with the Climate Data Operator (CDO) software [Schulzweida, 2019]. All the data was interpolated to a common 2.5 $\times$ 2.5 degrees grid using a first-order conservative remapping *remapcon*.

The 14 components of Earth's energy budget and two other variables studied in this thesis are listed in Table 2. For each component, the historical run and the RCP8.5 experiment were merged together and the decadal monthly means from the simulations were calculated. These were then used to determine the annual multimodel means of the simulated present-day energy budget and the projected changes in it, as well as the corresponding global averages. For this purpose, two 30-year averaging periods were chosen to be studied: a baseline period of 1981-2010 and a comparison scenario period at the end of the 21st century (2071-2100). The baseline period gives the simulated present-day energy budget and the changes in the studied variables between the periods (denoted with Δ) are expressed with respect to it. For example, the global

and annual multimodel mean warming of near-surface air between 1981-2010 and 2071-2100 is about 3.46 K.

For the projected changes, the intermodel correlation between temperature change ΔT and change in the other components along with the intermodel standard deviations were calculated. Furthermore, the ratio of multimodel mean to the intermodel standard deviation was examined. These were then used to study the intermodel consistency of the simulations. The results were obtained with the Grid Analysis and Display System (GrADS), a tool for handling and visualization of climate data (`http://cola.gmu.edu/grads/`).

Symbol	Component	CMIP5
T	Near-surface air temperature (2 m)	tas
$SW_{\downarrow TOA}$	TOA incident SW radiation	rsdt
$SW_{\uparrow TOA}$	TOA outgoing SW radiation	rsut
$LW_{\uparrow TOA}$	TOA outgoing LW radiation	rlut
$SW_{\downarrow}$	Surface downwelling SW radiation	rsds
$SW_{\uparrow}$	Surface upwelling SW radiation	rsus
$LW_{\downarrow}$	Surface downwelling LW radiation	rlds
$LW_{\uparrow}$	Surface upwelling LW radiation	rlus
$H_{\uparrow}$	Surface upward sensible heat flux	hfss
$LE_{\uparrow}$	Surface upward latent heat flux	hfls
$SW_{\uparrow TOA,cs}$	TOA outgoing clear-sky SW radiation	rsutcs
$LW_{\uparrow TOA,cs}$	TOA outgoing clear-sky LW radiation	rlutcs
$SW_{\downarrow cs}$	Surface downwelling clear-sky SW radiation	rsdscs
$SW_{\uparrow cs}$	Surface upwelling clear-sky SW radiation	rsuscs
$LW_{\downarrow cs}$	Surface downwelling clear-sky LW radiation	rldscs
CLT	Total cloud fraction	clt

Table 2: List of the symbols, their definitions and CMIP5 acronyms. The abbreviations: *TOA* top of the atmosphere, *SW* shortwave and *LW* longwave. Here clear-sky refers to radiation fluxes calculated assuming a cloud-free atmosphere.

4 Simulated present-day energy budget

A more detailed study of Earth's present-day energy budget is presented in this chapter. The results are obtained from the simulations described in the previous sections. Here, the first two sections examine the TOA radiation balance and briefly introduce effects of cloud forcing. The last section is divided into the study of the net surface radiation and the surface energy budget, respectively.

4.1 TOA net radiation

The TOA radiation balance is determined by the incident solar radiation, the reflected SW radiation and the outgoing LW radiation. We write

$$R_g = SW_{\downarrow TOA} - SW_{\uparrow TOA} - LW_{\uparrow TOA} \tag{1}$$

where R_g is the TOA net radiation. Energy balance is achieved if the incoming and outgoing energy fluxes cancel out (globally averaged $R_g = 0$). In case of a non-zero global mean R_g, the surface temperature would either rise or sink, depending on the sign of R_g.

Part of the incoming SW radiation is immediately reflected from the atmosphere and the surface. The spatial distribution of the TOA net SW radiation, the difference between incident and reflected SW fluxes, is depicted in Figure 2a. High latitudes receive less SW radiation than the equatorial region due to the curvature of Earth. Additionally, more SW radiation is reflected from the surface towards space due to higher surface albedo over the polar regions (Fig. 5). The TOA net SW radiation is also reduced over areas of higher cloud cover, for instance over the mid-latitude storm tracks, since clouds reflect a large fraction of the incident SW radiation.

Longwave radiation, or thermal radiation, is emitted by Earth's surface and the atmosphere. The emitted LW radiation flux is directly proportional to the fourth power of the temperature, and therefore areas of higher surface and atmospheric temperature emit more LW radiation. Figure 2b shows the spatial distribution of the annual mean TOA outgoing LW radiation. The colder polar regions emit less LW radiation than the warmer low latitude areas. However, the pole-to-equator gradient in the upwelling LW radiation is not as steep as that in the absorbed solar radiation due to the oceanic and atmospheric circulation transfering heat towards the higher latitudes. The outgoing LW radiation flux is strongest in the subtropics where the surface temperatures are high and the air is relatively dry, since clouds and water vapor reduce OLR.

The annual mean net radiation at the top of the atmosphere is depicted in Figure 2c. In the mid-to-high latitudes we have $R_g < 0$ and the net radiation is positive elsewhere, Sahara being an exception. OLR exceeds the net SW radiation at higher latitudes, which is balanced by poleward heat transfer. In Sahara, the surface reflectivity is high and the high temperatures and dry atmosphere cause larger OLR.

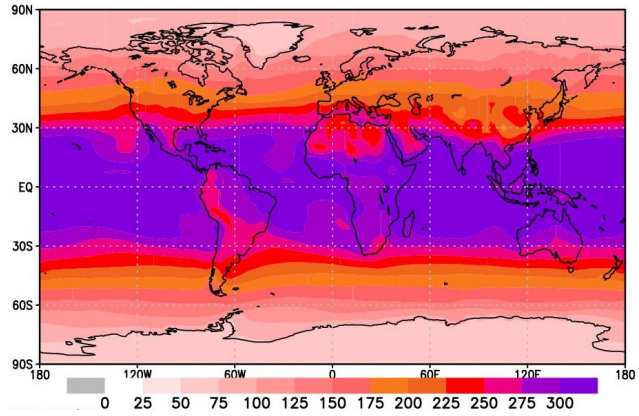

(a) TOA net SW radiation.

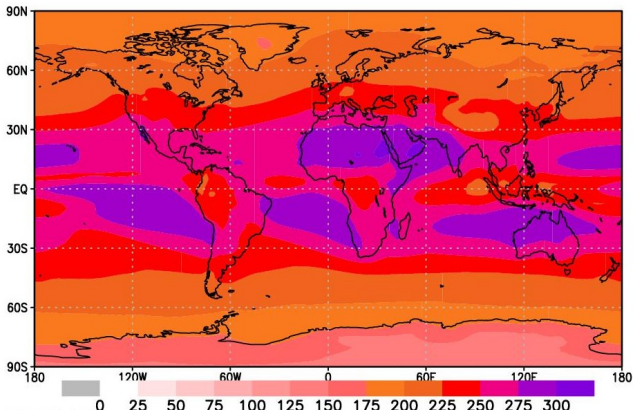

(b) TOA outgoing LW radiation.

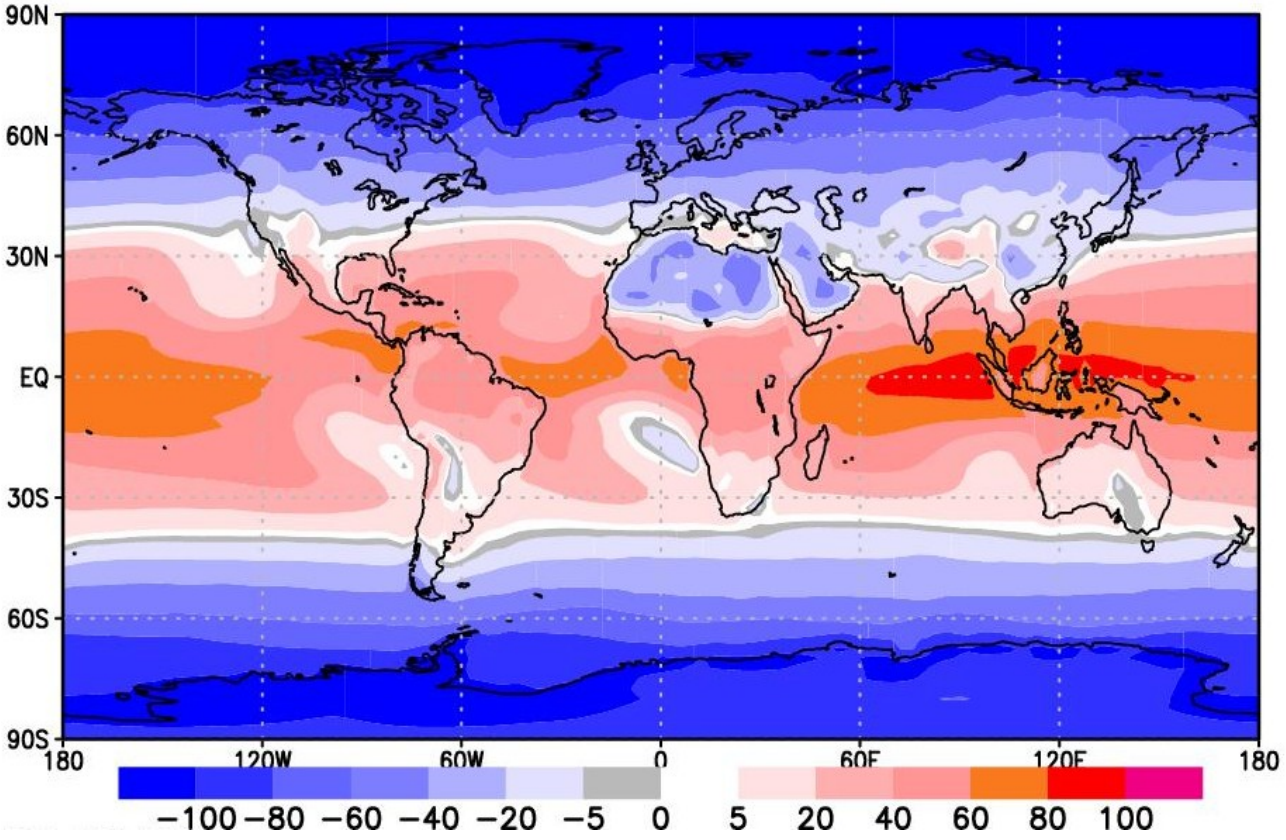

(c) TOA net radiation

Figure 2: Spatial distribution of the annual multimodel mean a) TOA net SW radiation, b) TOA OLR and c) TOA net radiation over the years 1981-2010. Units W/m^2.

The TOA net radiation is affected by the energy fluxes from the surface and the atmosphere. In Chapter 4.3, we will study the components of the surface energy budget. Before this, we will have a brief look into cloud forcing that also affects the TOA net radiation.

4.2 Cloud forcing

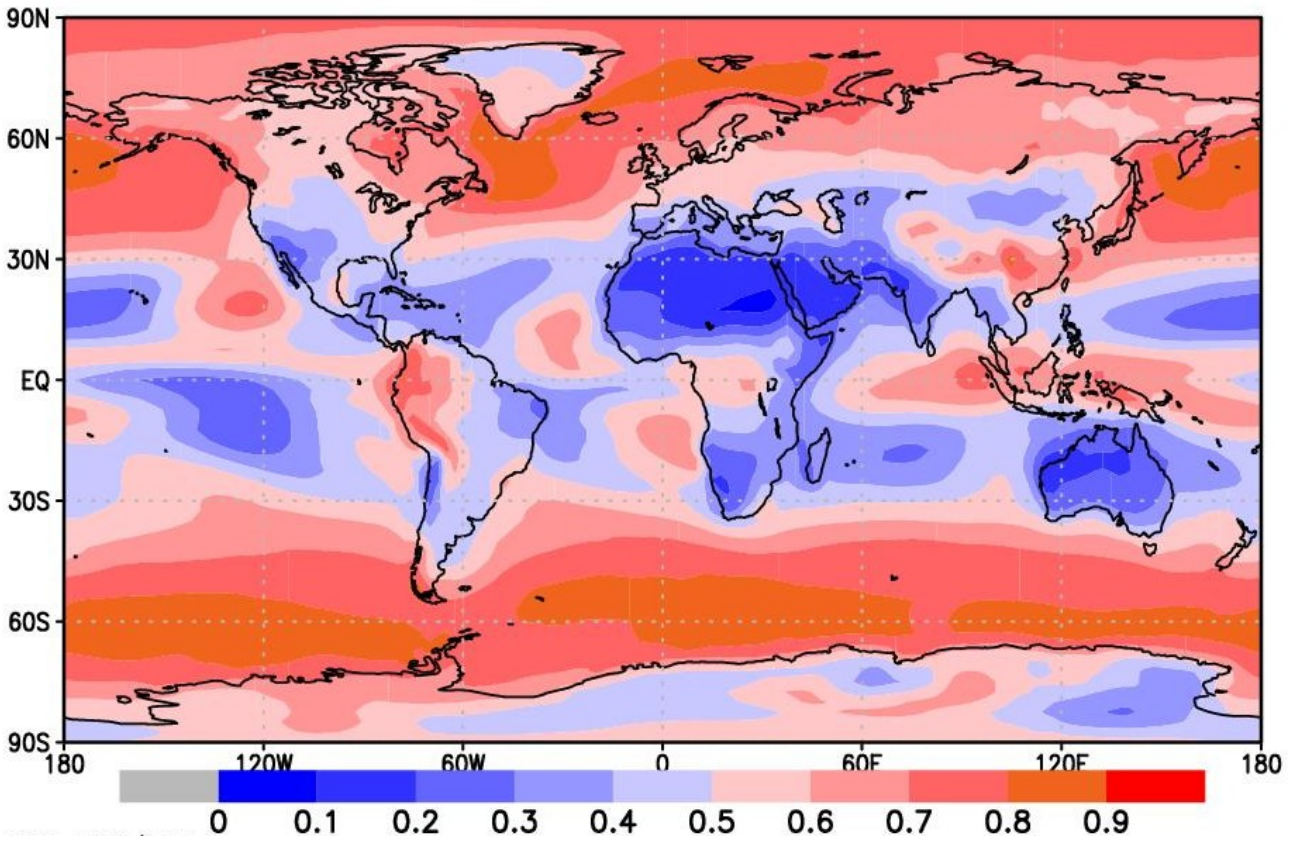

Figure 3: Spatial distribution of the annual multimodel mean cloud fraction over the years 1981-2010.

In current climate conditions, the fraction of Earth covered by clouds is about two thirds [Boucher et al., 2013]. Figure 3 shows the annual multimodel mean cloud fraction occurence. Clouds occur most frequently over the mid-latitude oceanic storm tracks and the tropical precipitation belts. The cloud coverage is low over deserts and the subtropical oceans.

Clouds play a double role in the TOA radiation balance: *i*) clouds reflect the incident SW radiation, having a cooling effect on Earth's climate and *ii*) less LW radiation is emitted to space by colder high-level cloud tops, having a warming effect. High clouds both reflect more SW radiation and emit less LW radiation to space, while low clouds mainly reflect solar radiation. The net cloud forcing at the TOA is [Räisänen, 2010]

$$\Delta R_{cloud} = R_g - R_g^{cs} = SW_{\uparrow TOA,cs} - SW_{\uparrow TOA} + LW_{\uparrow TOA,cs} - LW_{\uparrow TOA} \quad (2)$$

where *cs* means clear-sky conditions, or in other words, the absence of clouds. On average, more SW radiation is immediately reflected to space due to clouds (about 50 W/m^2) when compared to cloud-free conditions. Hence, the global mean SW cloud forcing is approximately -50 W/m^2 and the average LW cloud forcing is about 30 W/m^2, due to smaller LW flux to space in cloudy conditions (about -30 W/m^2) [Boucher et al., 2013]. Therefore, the net cloud forcing is -20 W/m^2 which means that clouds have a net cooling effect on Earth's current climate.

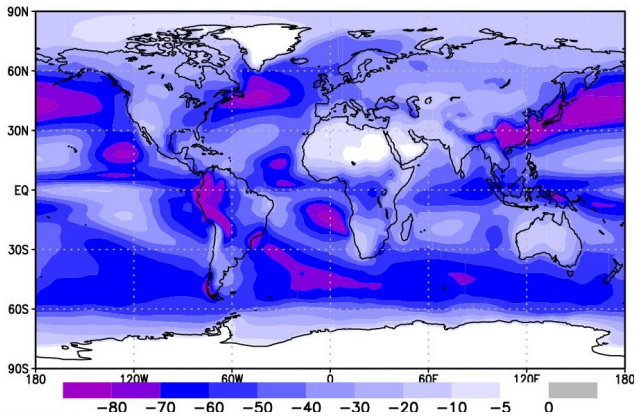

(a) SW cloud forcing.

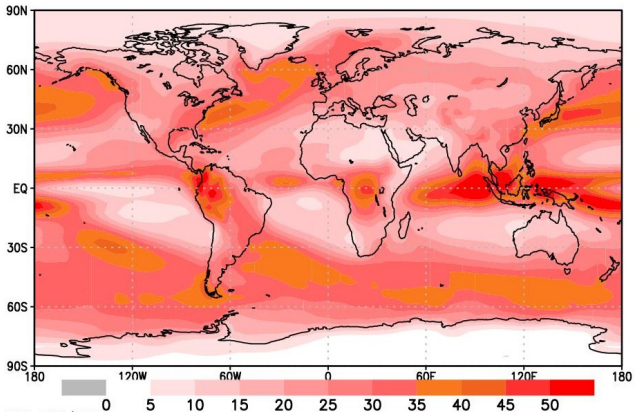

(b) LW cloud forcing.

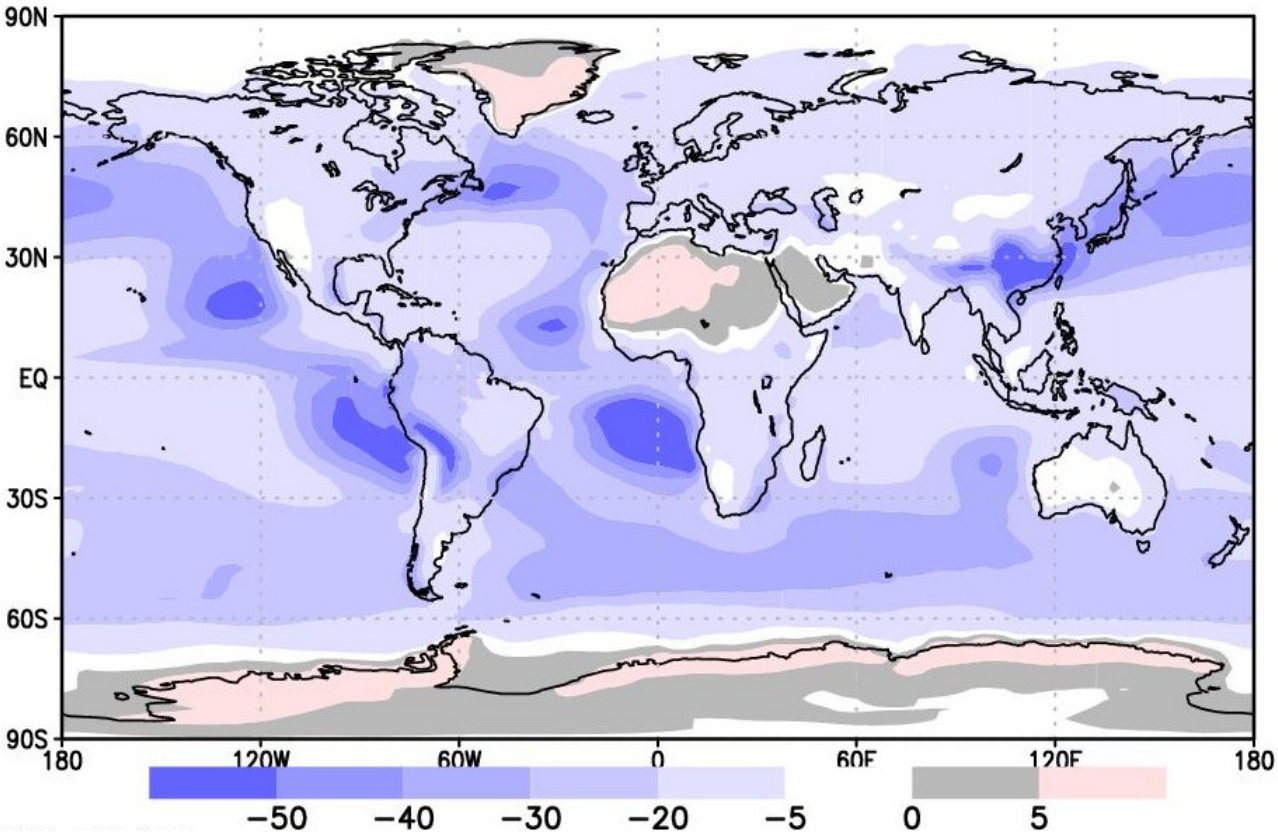

(c) Net cloud forcing.

Figure 4: Spatial distribution of the annual multimodel mean a) TOA net SW cloud forcing, b) TOA net LW cloud forcing c) TOA net cloud forcing over the years 1981-2010. Units W/m^2.

The annual multimodel mean SW, LW and net cloud forcing at the TOA are depicted in Figure 4. The net cloud forcing is slightly positive over the polar regions due to less incoming SW radiation and already high surface albedo, and it is negative over most of the other regions (Fig. 4c). Over the mid-latitude oceans, the net cloud forcing as well as the SW cloud forcing (Fig. 4a) is most negative. LW cloud forcing is more positive over regions with high clouds (Fig. 4b), for instance over the Tropical Pacific ocean, but reflection of SW radiation is also large in these areas.

The contribution of clouds to Earth's energy budget in the future projections still poses a challenge for climate modeling [Boucher et al., 2013]. Changes in climate lead to different climate feedbacks including cloud feedback, which among other things depends on the change in cloud fraction and properties. Hence, the brief summary of cloud forcing presented here is relevant to understanding the processes affecting Earth's energy fluxes in the current and simulated future climate.

4.3 Surface energy fluxes

4.3.1 Surface net radiation

For the net surface radiation we write

$$R = SW_{\downarrow} - SW_{\uparrow} - (LW_{\uparrow} - LW_{\downarrow}) \tag{3}$$

where the first two terms on the right contribute to the surface net SW radiation, and the last two terms to the surface net LW radiation. The part of the incident solar radiation that is not reflected from or absorbed by the atmosphere reaches the surface. The surface reflects part of this downwelling SW radiation back to space but, on average, nearly 50 % of the solar radiation is absorbed at the surface (Fig. 1).

Surface albedo α measures the fraction of SW radiation that is reflected at the surface. Figure 5 shows the spatial distribution of the annual mean surface albedo. The reflectivity is higher over the continents than over the oceans ($\alpha \leq 0.1$). The ice and snow cover have high surface albedos ($0.5 \leq \alpha \leq 0.9$) but seasonal variations occur. Other important types of surface are vegetation ($0.1 \leq \alpha \leq 0.3$) and deserts ($0.3 \leq \alpha \leq 0.4$). The global average surface albedo is approximately 0.13 (Fig. 1). Similarly, the planetary albedo, defined as the fraction of incoming SW radiation that is reflected from Earth, is about 0.3.

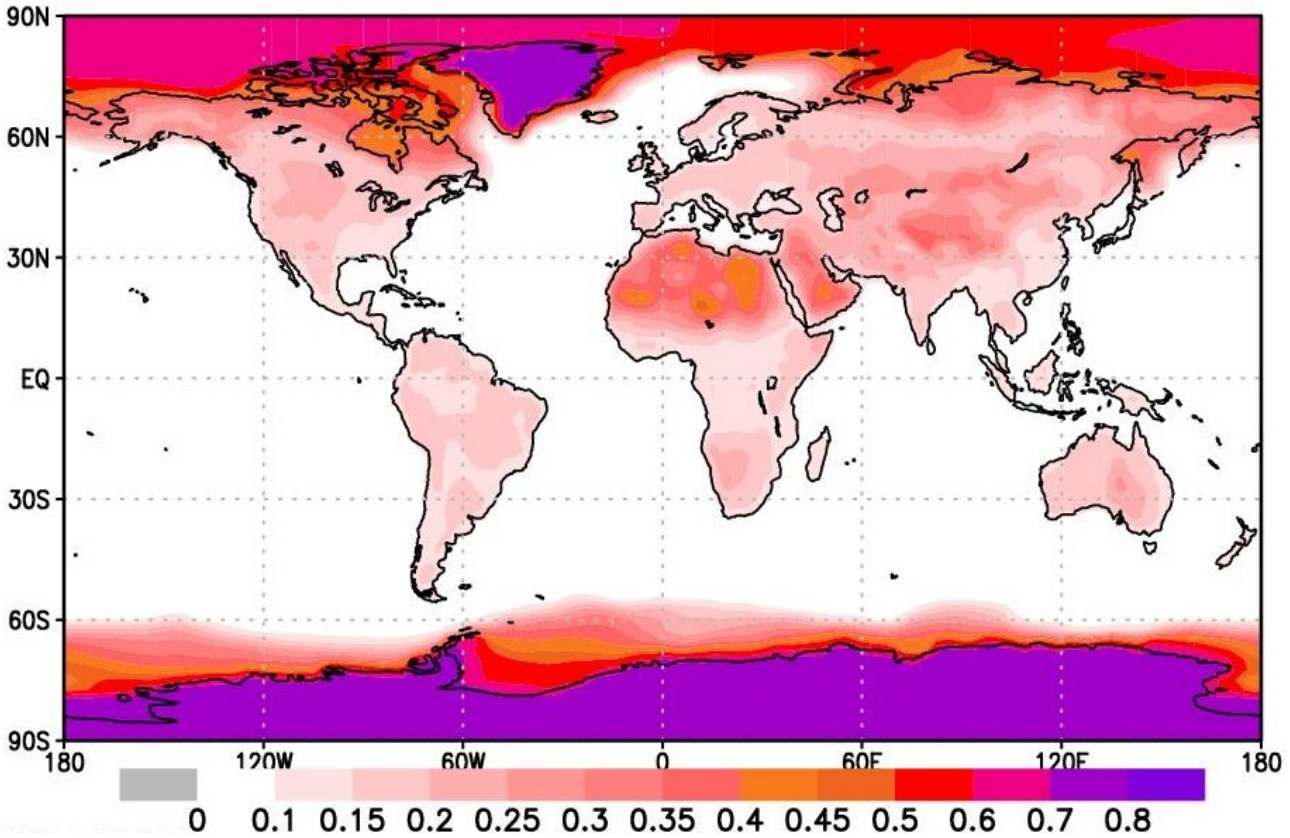

Figure 5: Spatial distribution of the annual multimodel mean surface albedo over the years 1981-2010.

The spatial distribution of the annual mean surface net SW radiation is depicted in Figure 6a. The latitudinal distribution is similar to Figure 2a due to Earth's curvature, but the effect of the atmosphere and the reflection from the surface can be seen here. The magnitude of the downwelling SW radiation is high over deserts and other areas with relatively clear sky. Clouds reduce the SW radiation to the surface, which can be seen over the oceans at higher latitudes, for instance. Due to the higher surface albedo over deserts and the polar regions (Fig. 5), a major part of the downward SW radiation is immediately reflected. The reflection is weaker over the oceans than the continents, because the surface albedo is significantly smaller.

Figure 6b shows the spatial distribution of the annual mean surface net LW radiation. At higher latitudes, the surface temperatures are low, and therefore upwelling LW radiation is smaller. Similarly, the ocean surface temperatures are lower when compared to land areas because of strong evaporation over the oceans. The surface net LW radiation is large over deserts and other areas with relatively dry air. Atmospheric re-radiation mostly emitted by the lower atmosphere is large over areas with high atmospheric water vapor content and cloud coverage.

The spatial distribution of the annual mean surface net radiation can be seen in Figure 6c.

The net radiation is negative in the polar regions and positive elsewhere. In the lower latitudes, the net radiation is larger over the oceans than over the land areas. In Sahara, the emitted LW radiation and the reflected SW radiation fluxes are stronger due to high surface temperatures and surface albedo, resulting in weaker net radiation.

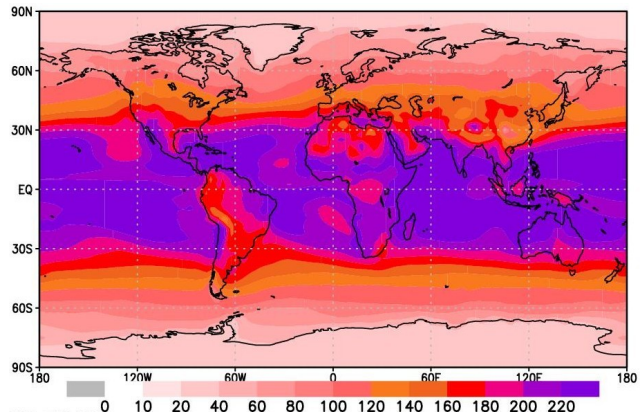

(a) Surface net SW radiation.

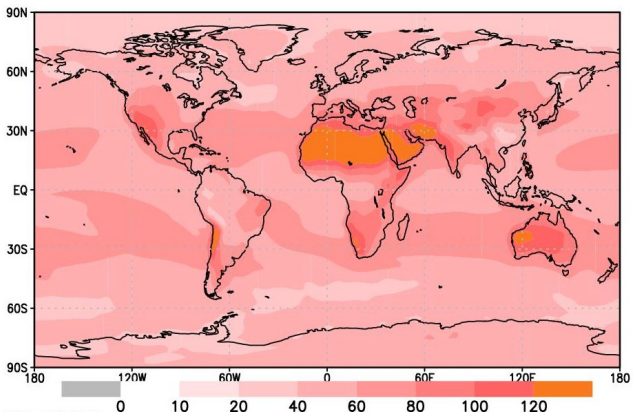

(b) Surface net LW radiation (positive upward).

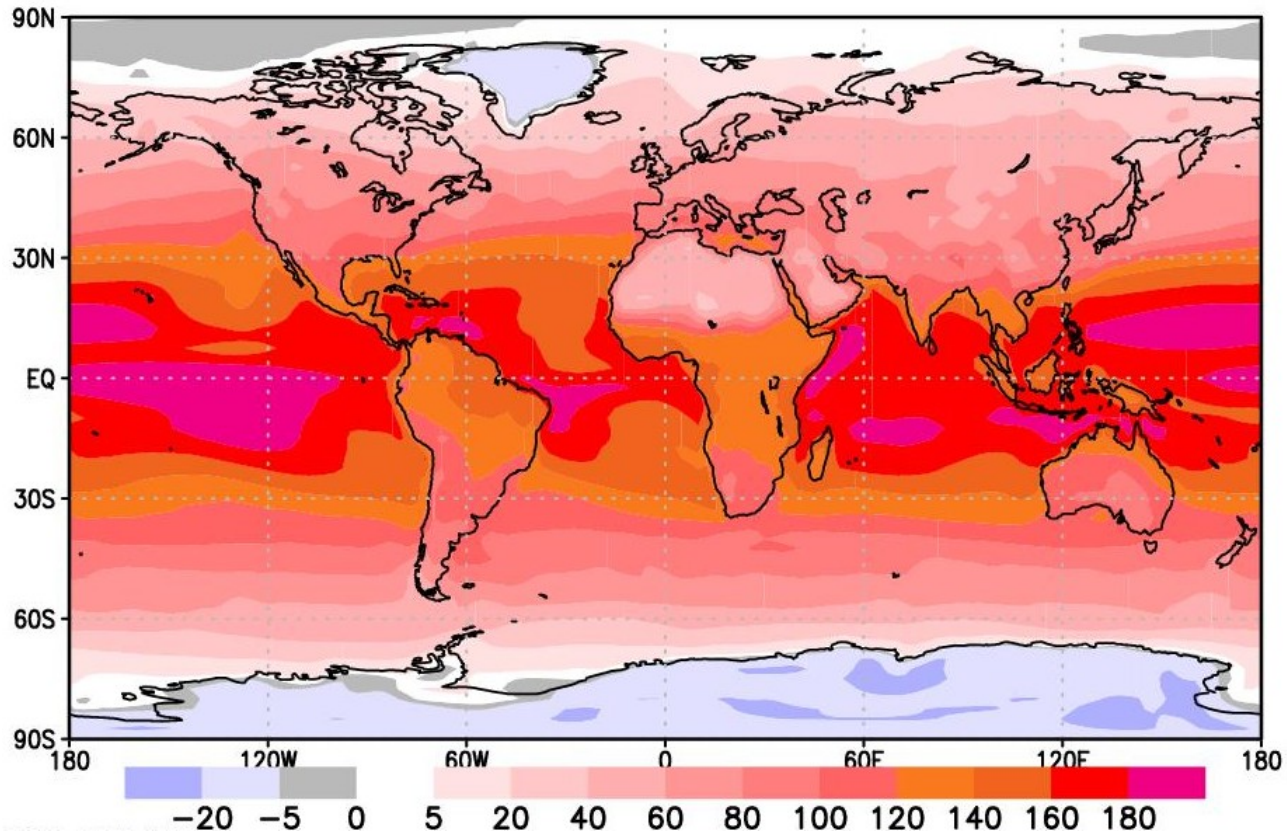

(c) Surface net radiation.

Figure 6: Spatial distribution of the annual multimodel mean a) surface net SW radiation, b) surface net LW radiation (defined here as positive upward) and c) surface net radiation over the years 1981-2010. Units W/m^2.

In addition to thermal radiation, turbulent heat fluxes transfer energy between the surface

and the atmosphere. In order to present Earth's surface energy budget, these non-radiative components are first studied. Part of the net surface radiation energy (Fig. 6c) is distributed between the latent heat flux and the sensible heat flux, as we will see in the next section.

4.3.2 Turbulent heat fluxes and the surface energy budget

Phase changes of a substance involve energy that is either absorbed or released, depending on the direction of transition, called latent heat. Phase changes of water from liquid or solid to gas or vice versa transfer heat energy between the surface and the atmosphere. Evaporation cools the land and sea surface, and the condensation of water vapor in the atmosphere releases latent heat which in turn warms the air. Evaporation from both the surface and vegetation, *evapotranspiration* [Neelin, 2011], is the dominating factor in the latent heat flux over land.

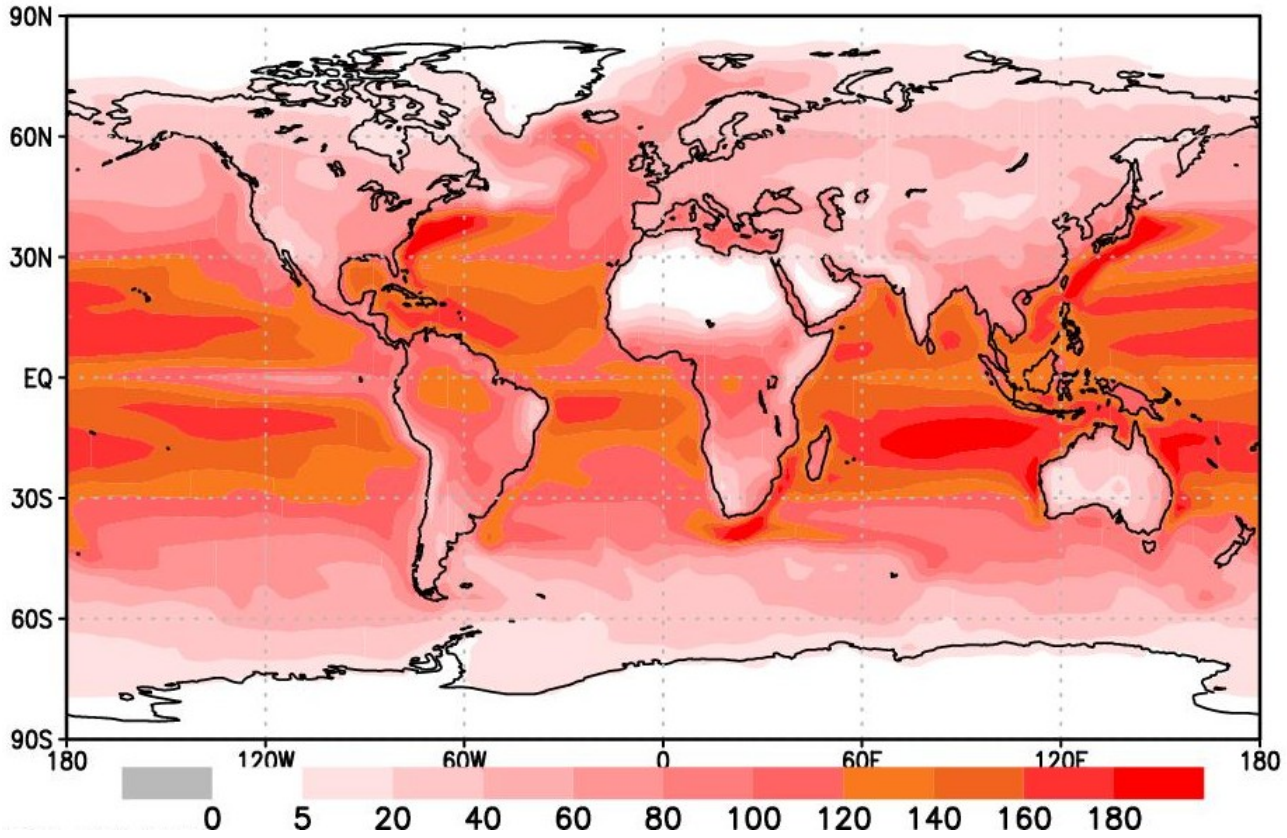

Figure 7: Spatial distribution of the annual multimodel mean latent heat flux over the years 1981-2010. Units W/m^2.

The spatial distribution of the annual mean latent heat flux is depicted in Figure 7. Since the magnitude of $LE_{\uparrow}$ depends on the surface temperature and moisture, the flux is greatest over the warm oceans around the equator. The oceans store heat energy more efficiently than the land areas, and the ocean currents move warm waters poleward. For instance, in the North Atlantic Ocean $LE_{\uparrow}$ exceeds the latent heat flux over the continents at the same latitude.

$LE_{\uparrow}$ is smaller over the land areas. In dry areas, such as Sahara, there is little to none moisture and the latent heat flux is modest. In the polar regions, the energy required for phase transitions is scarce. Additionally, the maximum possible amount of water vapor in the air depends on the temperature so that cold air can hold less water vapor. Over the tropical rainforests, the latent heat flux is great due to the evapotranspiration process.

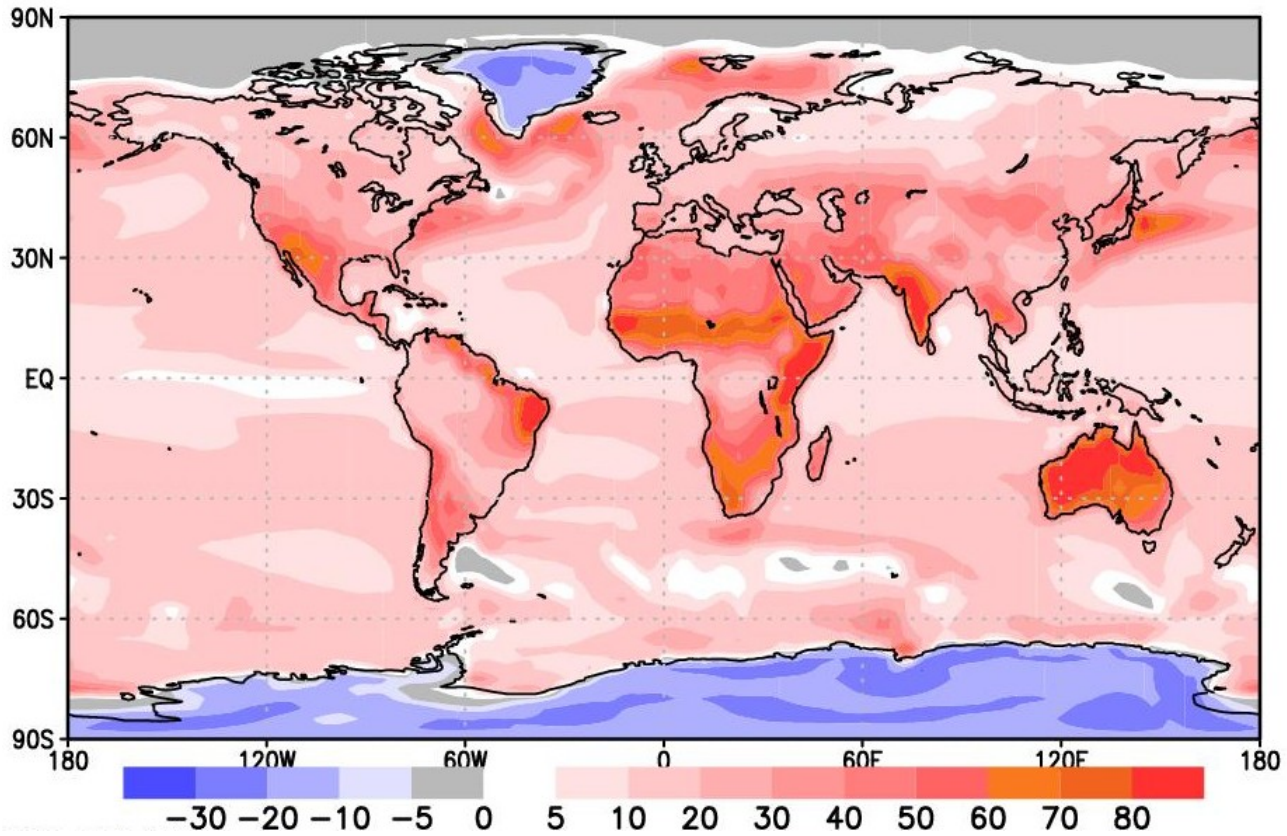

Figure 8: Spatial distribution of the annual multimodel mean sensible heat flux over the years 1981-2010. Units W/m^2.

Figure 8 shows the spatial distribution of the annual mean sensible heat flux. In short, sensible heat transfer occurs when air molecules come in contact with the warm surface which causes the upward movement of warmer air [Neelin, 2011]. The magnitude of $H_{\uparrow}$ depends on the temperature difference between the surface and the air above it. Over the oceans, $H_{\uparrow}$ is relatively small because most of the radiation energy (Fig. 6c) goes to evaporation. Over some sea areas, for instance in the North Atlantic, $H_{\uparrow}$ is greater due to the temperature difference between the colder air and the warm ocean currents.

Over land, $H_{\uparrow}$ is smaller at higher latitudes. The sensible heat flux is negative in the polar regions since the warmer atmosphere loses energy to the surface, while at lower latitudes, $H_{\uparrow}$ is large due to larger surface net radiation flux (Fig. 6c). Over dry areas, such as Sahara, the high surface temperatures and smaller $LE_{\uparrow}$ due to lack of soil moisture result in greater $H_{\uparrow}$.

The surface energy budget is [Räisänen, 2010]

$$R = H_{\uparrow} + LE_{\uparrow} + G + \Delta F \tag{4}$$

where G is the energy stored per unit horizontal area and ΔF is the horizontal transfer of energy associated with, for instance, the oceanic circulation. Figure 9 shows the spatial distribution of annual mean $R - H_{\uparrow} - LE_{\uparrow}$, defined as positive downward. Over land, ΔF becomes negligible and the annually averaged G is very close to zero [Räisänen, 2010], and therefore the net energy flux is relatively small. The spatial distribution of the net atmosphere-ocean heat exchange can be seen in Figure 9. In the northern North Atlantic, for instance, the net heat flux is negative and the warmer sea loses heat to the colder atmosphere, while in the tropics the ocean heat uptake is strong.

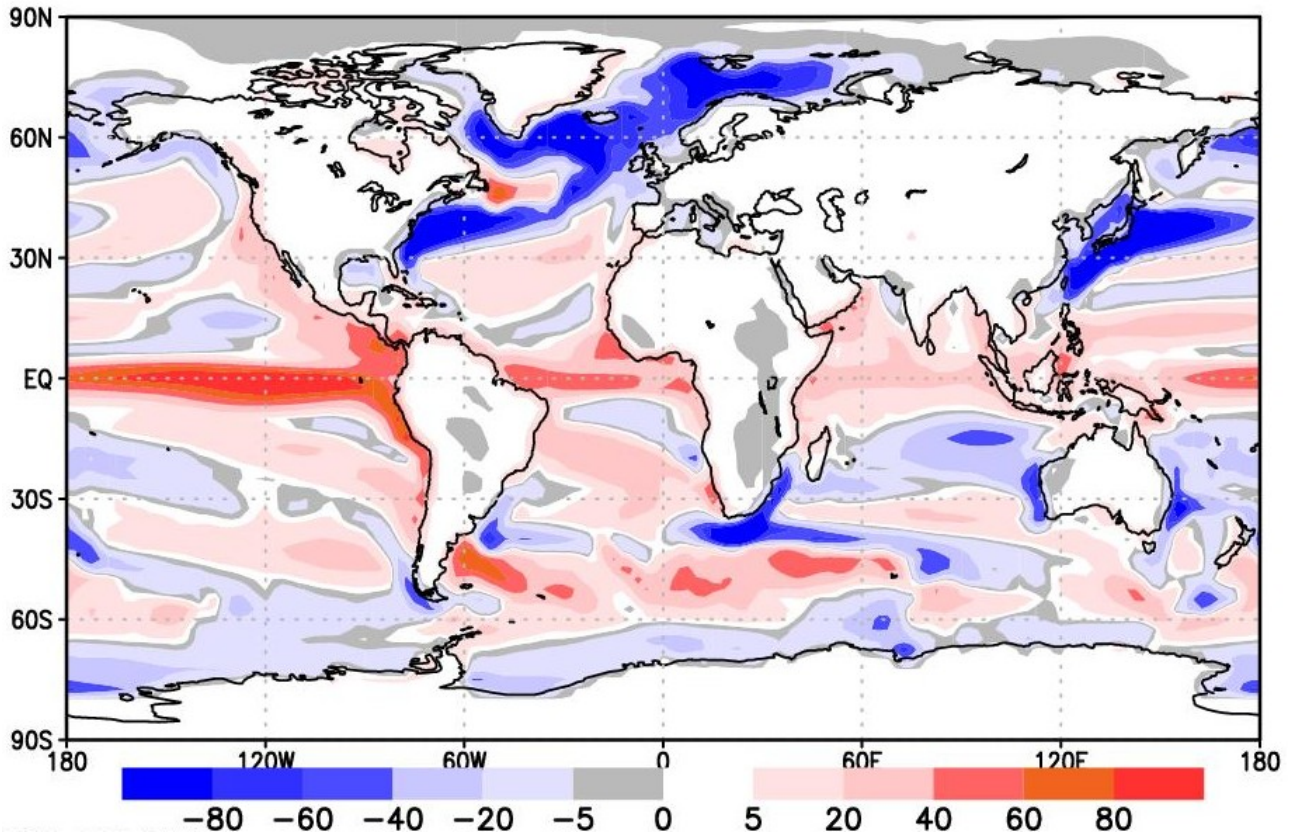

Figure 9: Spatial distribution of the annual multimodel mean $R - H_{\uparrow} - LE_{\uparrow}$ over the years 1981-2010. Units W/m^2.

5 Simulated changes in the energy budget

Increases in atmospheric GHGs due to human activities cause an energy imbalance at the top of the atmosphere, leading to changes in the energy fluxes, various climate feedbacks, and changes

in Earth's mean temperature. In this chapter, the simulated changes in the components of the energy budget, clouds and surface temperature between the scenario period (2071-2100) and the baseline period (1981-2010) are studied. First, the globally averaged changes are presented, and then the spatial distributions of the annual multimodel means of changes are examined.

5.1 Globally averaged changes

Component	Present-day	Change	Units
T	287.3	3.5	K
$SW_{\downarrow TOA}$	341.3	0.03	W/m^2
$SW_{\uparrow TOA}$	102.2	-3.8	W/m^2
$LW_{\uparrow TOA}$	238.2	1.9	W/m^2
$SW_{\downarrow}$	190.7	-1.4	W/m^2
$SW_{\uparrow}$	25.0	-1.9	W/m^2
$LW_{\downarrow}$	338.7	23.5	W/m^2
$LW_{\uparrow}$	397.2	18.4	W/m^2
$H_{\uparrow}$	19.9	-1.0	W/m^2
$LE_{\uparrow}$	86.2	4.9	W/m^2
$SW_{\uparrow TOA,cs}$	53.8	-3.1	W/m^2
$LW_{\uparrow TOA,cs}$	262.9	1.1	W/m^2
$SW_{\downarrow cs}$	249.5	-3.1	W/m^2
$SW_{\uparrow cs}$	31.1	-2.4	W/m^2
$LW_{\downarrow cs}$	312.5	26.8	W/m^2
CLT	58.4	-0.9	%

Table 3: The rounded global and annual multimodel means for the 16 variables. The second column: the simulated present-day values. The third column: the simulated change between the baseline period (1981-2010) and the RCP8.5 scenario period (2071-2100).

The simulated present-day global multimodel annual means for the 16 variables and changes in them are listed in Table 3. For the second column, we can compare the magnitude of the present-day TOA radiation fluxes and the components of the surface energy budget with Figure 1. Most of the simulated global averages are within the uncertainty ranges given in Figure 1, while $SW_{\uparrow TOA}$, $SW_{\downarrow}$ and $LE_{\uparrow}$ are slightly larger. However, the study of these differences is

beyond the scope of this thesis, and therefore it is not further explored here.

We first note that the global average temperature change is 3.5 K. The average change in $SW_{\downarrow TOA}$ (0.03 W/m^2) is negligible when compared to other energy fluxes. The main effects affecting the SW radiation fluxes are the change of clouds, reduced ice and snow cover and increase in atmospheric water vapor content, while for the LW radiation the changes in surface temperature and in the atmospheric composition are the main factors [Räisänen, 2016].

The global mean $\Delta SW_{\uparrow TOA}$ (-3.8 W/m^2) and $\Delta SW_{\uparrow TOA,cs}$ (-3.1 W/m^2) are both negative. Hence, less SW radiation is reflected to space in both cloudy and cloud-free conditions. This effect is partly due to changes in atmospheric composition, since more SW radiation is absorbed by increased water vapor in the atmosphere, and additionally, the reduced surface albedo over high latitudes contributes to the changes in reflected SW fluxes (Fig. 14) [Donohoe et al., 2014]. Changes in the cloud cover explain the difference between the cloudy and the cloud-free components: the annual mean cloud cover is reduced over most low-to-mid latitude areas, as can be seen later in Chapter 5.3 (Fig. 11). Hence, on average the reflection from clouds is reduced and $|\Delta SW_{\uparrow TOA}| > |\Delta SW_{\uparrow TOA,cs}|$.

The global mean changes in both OLR components $\Delta LW_{\uparrow TOA}$ (1.9 W/m^2) and $\Delta LW_{\uparrow TOA,cs}$ (1.1 W/m^2) are positive, and the increase is associated with warming of the surface and the atmosphere (the Planck feedback). Increase in GHGs make the atmosphere less transparent to LW radiation, and therefore the change in OLR is significantly smaller when compared to changes in the surface LW fluxes. For the net radiation change at the top of the atmosphere, the global average for ΔR_g is about 1.9 W/m^2, resulting in an accumulation of energy in the climate system, mainly as increased ocean heat content [Rhein et al., 2013].

We note that $|\Delta SW_{\uparrow TOA}| > \Delta LW_{\uparrow TOA}$, and similarly for the clear-sky components. Likewise, other studies of simulated future projections have found that the dominating factor in sustaining the TOA energy imbalance, and therefore causing additional global warming, is increase in the net absorbed SW radiation, instead of reduced OLR due to increased GHGs [Donohoe et al., 2014]. As already mentioned, increased water vapor in the atmosphere and the reduced ice and snow cover both enhance the absorption of incident SW radiation, and these feedbacks, together with reduced cloudiness, are the likely cause of the resulting changes in the SW fluxes.

At the surface, the global mean $\Delta SW_{\downarrow}$ (-1.4 W/m^2), $\Delta SW_{\downarrow cs}$ (-3.1 W/m^2), $\Delta SW_{\uparrow}$ (-1.9 W/m^2) and $\Delta SW_{\uparrow cs}$ (-2.4 W/m^2) are all negative. Similarly to the TOA components, the first two of these are due to stronger absorption of SW radiation in the atmosphere by increased water vapor, and the difference is again explained by the reduced cloud cover: the downward SW radiation changes less in the cloudy conditions because the reflection from clouds is re-

duced. The last two components mainly reflect the effects of reduced ice and snow cover as the temperature rises. Less SW radiation is reflected at the surface due to changes in the surface albedo, since snow and ice have a high albedo compared to other types of surface.

The upward thermal radiation is increased by about 18.4 W/m^2 due to surface warming, and both of the atmospheric re-radiation components $\Delta LW_{\downarrow}$ (23.5 W/m^2) and $\Delta LW_{\downarrow cs}$ (26.8 W/m^2) are strongly positive. Most of the atmospheric re-radiation occurs from the lower atmospheric layers, where the temperature change is closely similar to the pattern of surface warming [Zhao et al., 1994]. Additionally, increase in GHGs makes the atmosphere less transparent to LW radiation and stronger absorption and emissions occur. Hence, the change in net upward LW flux is -5.1 W/m^2, and the net cooling of the surface becomes weaker. $\Delta LW_{\downarrow}$ is smaller than the cloud-free component due to reduced cloud cover. For the LW radiation components, the TOA radiation fluxes change less than the surface fluxes due to the atmosphere.

The global mean change in the net surface radiation balance (ΔR) is about 5.7 W/m^2, causing additional warming of the surface and leaving more energy to be distributed between $H_{\uparrow}$ and $LE_{\uparrow}$. The global average $\Delta H_{\uparrow}$ is approximately -1.0 W/m^2, while the global mean $\Delta LE_{\uparrow}$ (4.9 W/m^2) is positive and reflects stronger evaporation from the surface as the global mean temperature rises, according to the Clasius-Clapeyron relation. The global mean for $\Delta(R - H_{\uparrow} - LE_{\uparrow})$ is approximately 1.7 W/m^2, which is heat stored to the oceans.

The global means from Table 3 give an insight to the future changes but the patterns of change might vary greatly over different areas, and therefore we will study the spatial distribution of the simulated annual mean changes in the following sections. First, changes in the near-surface air temperature are examined.

5.2 Changes in the surface temperature

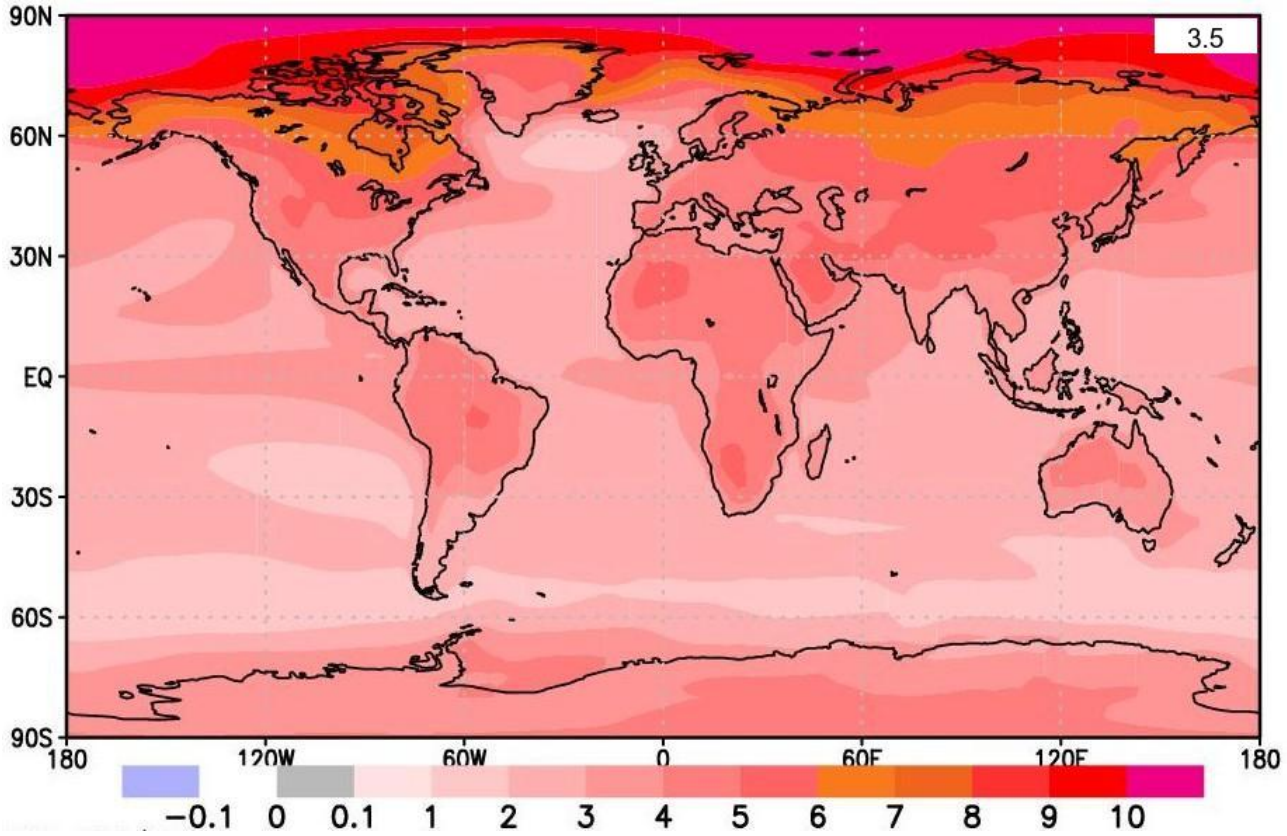

Figure 10: Spatial distribution of the annual multimodel mean of near-surface air temperature change for 2071-2100 (compared to 1981-2010 base period). Top-right corner: the global mean of ΔT from Table 3. Units K.

Figure 10 shows the spatial distribution of ΔT. The annually averaged surface temperature increases everywhere but regional variations in the warming pattern occur. Various physical processes affect the pattern of surface warming, including vegetation and snow/ice cover changes, ocean heat storage and changes in the soil moisture content, to name a few. The three key features in Figure 10 are:

- *The land-ocean contrast in the low-to-mid latitudes.* On average, the surface temperature change is larger over land compared to oceans. Even though the oceans have higher heat capacity, the difference is partly due to larger increase in latent heat flux over the oceans (Fig. 18a), which effectively cools the sea surface, and reduced soil moisture in drying land areas, leading to decrease in evaporation [Collins et al., 2013].

- *The polar amplification.* Various studies have found that the projected surface warming is largest in the northern high latitudes [Collins et al., 2013]. We see from Figure 10 that, in the Arctic latitudes, the change in surface temperature is on average over 2 to 3 times larger compared to other areas. The initial warming is amplified by the snow/ice feedback due to snow and sea ice cover reductions [Holland and Bitz, 2003, Collins et al., 2013]. In the Antarctic, due to low temperatures and the size of the ice sheet, the changes in the surface albedo are small (Fig. 14), and consequently amplified warming does not occur in the southern polar regions [Collins et al., 2013].

- *Variations in the sea surface temperature change in the low-to-mid latitudes* (SST). The warming is smallest in the northern North Atlantic and the Southern oceans due to the deep ocean mixing and, in the North Atlantic, due to the weakening of the thermohaline circulation, while ΔT is largest in the Tropical Pacific at the equator and near coastlines [Collins et al., 2013].

The following sections will study the changes in energy fluxes and cloud cover associated with the warming, and we will consider the relationship between the temperature change and the change in other variables more thoroughly.

5.3 Changes in the TOA net radiation and clouds

Since the change in net LW and SW fluxes at the top of the atmosphere depend, among other factors, on changes in cloud cover, we will first study briefly the spatial distribution of total cloud fraction change depicted in Figure 11. The main changes in cloud coverage are:

- Reduced cloud cover in the low-to-mid latitudes, except over the equatorial and Eastern Pacific oceans (Fig. 11) [Collins et al., 2013].

- Increases in cloudiness at higher latitudes (Fig. 11) [Collins et al., 2013].

- The cloud top rising associated with the warming [Meehl et al., 2013].

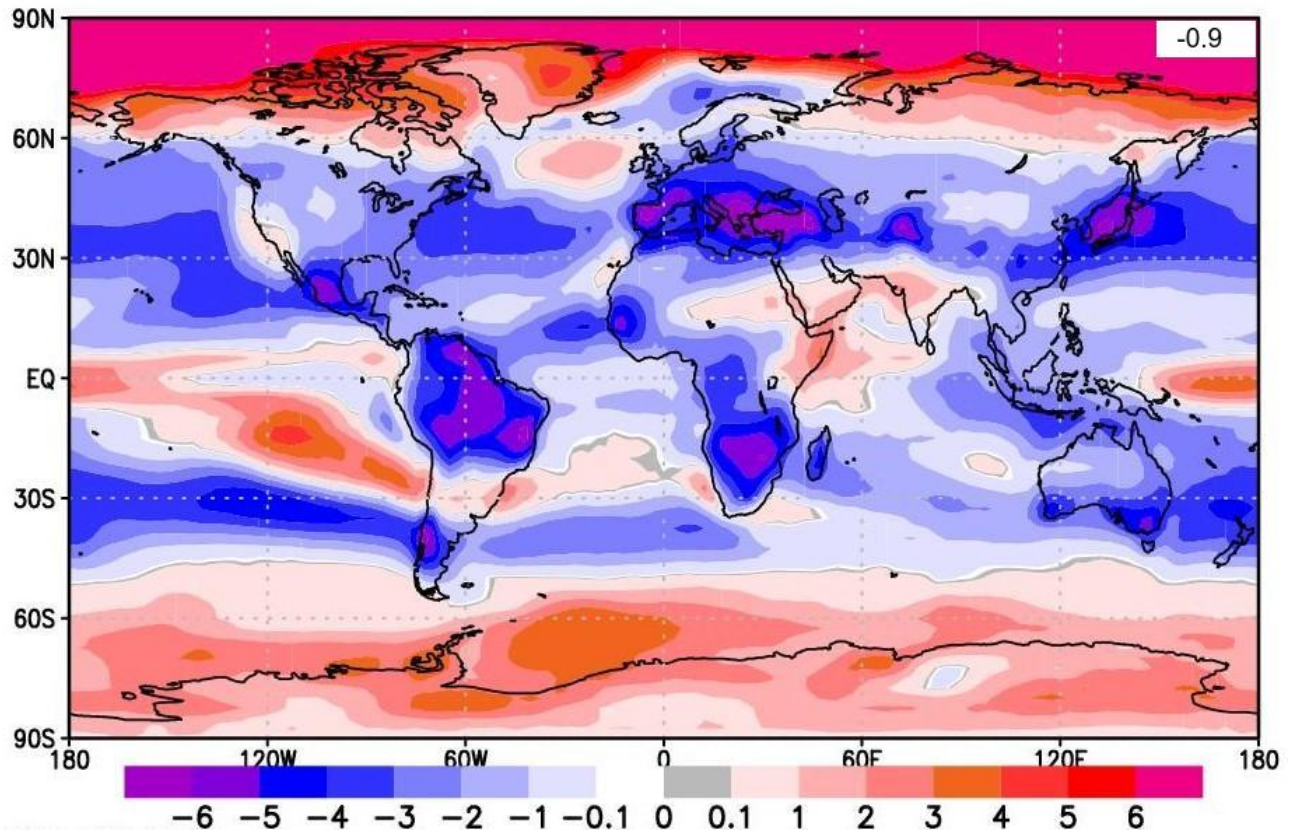

Figure 11: Spatial distribution of the annual multimodel mean of changes in cloud cover for 2071-2100 (compared to 1981-2010 baseline period). Units %.

The spatial distribution of the change in TOA net radiation is shown in Figure 12c. On average, the change is mostly positive and the energy imbalance at the top of the atmosphere increases compared to the baseline period. The changes in the TOA incident solar radiation are negligible compared to other energy fluxes, and therefore the pattern of change is not presented here. Next, the change in TOA net SW flux and OLR are studied separately. In addition to changes in cloud cover, the changes in TOA net SW radiation are affected by increase in atmospheric water vapor content and changes in snow and ice cover at higher latitudes [Collins et al., 2013]. Figure 12a shows the spatial distribution of the TOA net SW radiation change. On average, the absorption of incident SW radiation increases, and less SW radiation is reflected to space [Donohoe et al., 2014]. In the low-to-mid latitudes, where the change is positive, we see that the downward SW flux increases more over the areas with reduced cloud cover (Fig. 11) [Collins et al., 2013]. In other words, the reflection of SW radiation from clouds is reduced over these regions.

In the northern high latitudes, the TOA net SW radiation increases due to reduced snow and ice cover. Less SW radiation is reflected from the surface and, as already mentioned in the previous section, the warming in higher latitudes is amplified by the snow/ice feedback (Fig.

10). The changes in snow and ice cover more than compensate the effect of increased cloud cover on SW radiation in the higher latitudes (Fig. 11). Over part of the Southern ocean, northern North Atlantic and parts of the equatorial and Eastern Pacific ocean, the average change in TOA net SW flux is negative. The absorption of SW radiation decreases in these areas due to increase in cloud cover and reflection from clouds (Fig. 11).

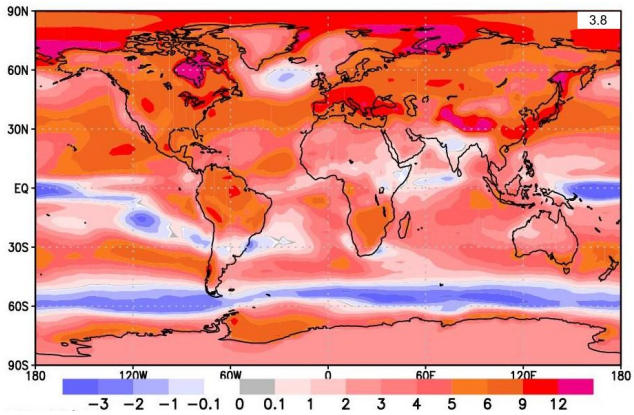

(a) TOA net SW radiation change.

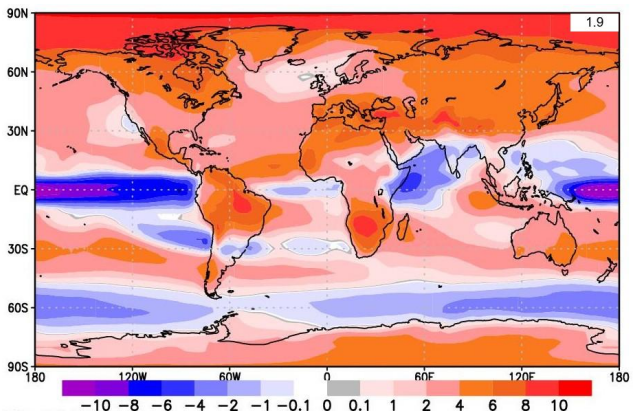

(b) OLR change (positive upward).

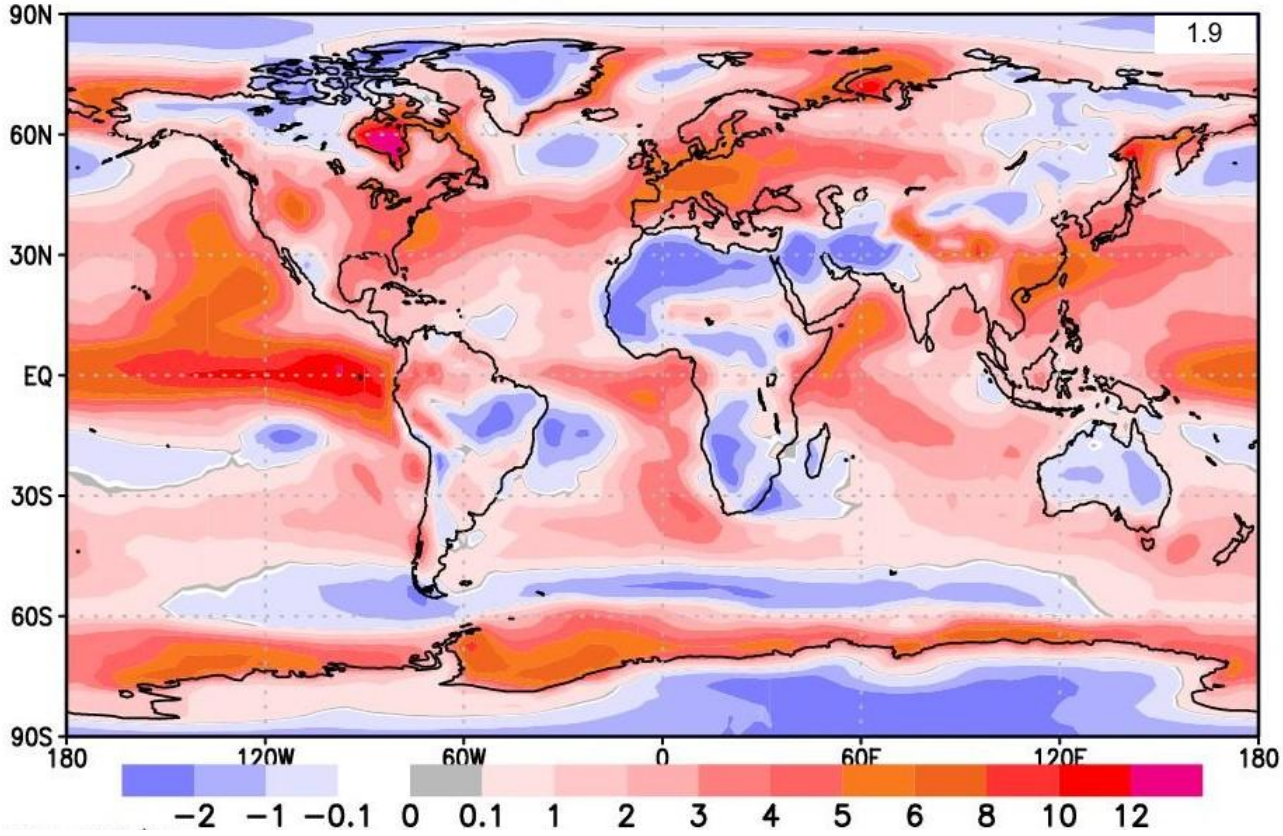

(c) TOA net radiation change

Figure 12: Spatial distribution of the annual multimodel mean of a) TOA net SW radiation change, b) TOA OLR change (defined here as positive upward) and c) TOA net radiation change for 2071-2100 (compared to 1981-2010 base period). Units W/m^2.

The spatial distribution of the change in TOA outgoing LW radiation is depicted in Figure 12b, where the flux is defined as positive upward. On average, there is an increase of the emitted LW radiation by surface and atmosphere towards space. Because OLR depends on surface and atmospheric temperatures, there are similarities between the pattern of surface warming (Fig. 10) and the changes in OLR (Fig. 12b). However, the net LW flux at TOA is affected largely by GHGs and also by clouds, explaining the differences between Figures 10 and 12b. The strong absorption of thermal radiation by GHGs in the atmosphere reduces OLR, and hence the change in OLR is relatively small compared to $\Delta LW_{\uparrow}$ (Fig. 16a) and the net surface warming. OLR increases over regions of reduced cloud cover, since more LW radiation is emitted to space from warmer atmospheric layers. On the other hand, in convective regions, such as the Tropical Pacific, the effect of cloud top rising reduces the OLR emissions towards space [Collins et al., 2013].

We study briefly the spatial distributions of the changes in SW, LW and net cloud forcing. These are depicted in Figures 13a, 13b and 13c, where a positive change in cloud forcing (CF) leads to additional warming of Earth's climate and vice versa. In the low-to-mid latitudes, over the areas of reduced cloud cover, the SW cloud forcing becomes less negative (Fig. 13a). Less SW radiation is reflected from clouds towards space, and correspondingly more is absorbed by the surface and the atmosphere. Over the same regions, the LW cloud forcing decreases and more LW radiation is emitted to space (Fig. 13b). On the other hand, over areas of increased cloud cover or rising cloud top (convective regions), the SW cloud forcing decreases (Fig. 13a) and the LW cloud forcing increases (Fig. 13b) due to stronger reflection of SW radiation and less LW radiation being emitted from higher layers, respectively.

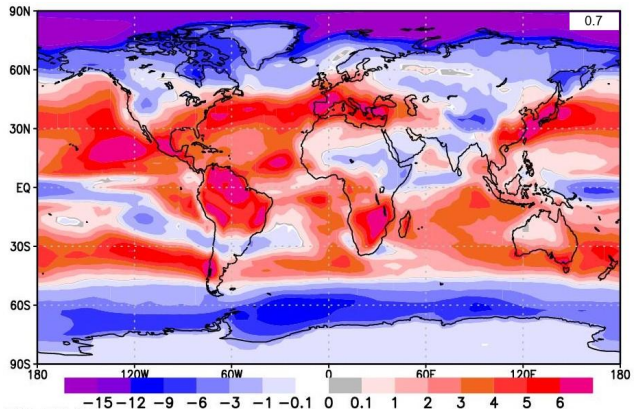

(a) Change in SW cloud forcing.

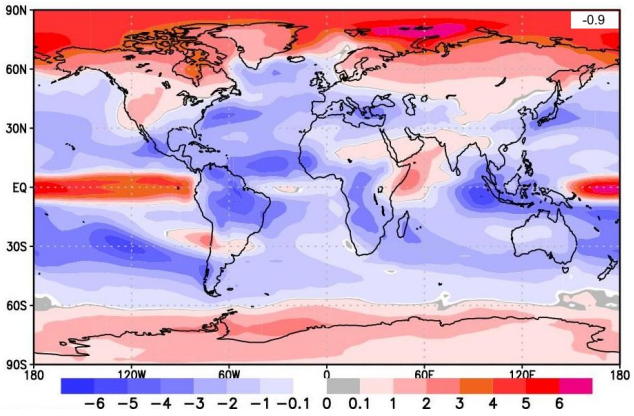

(b) Change in LW cloud forcing.

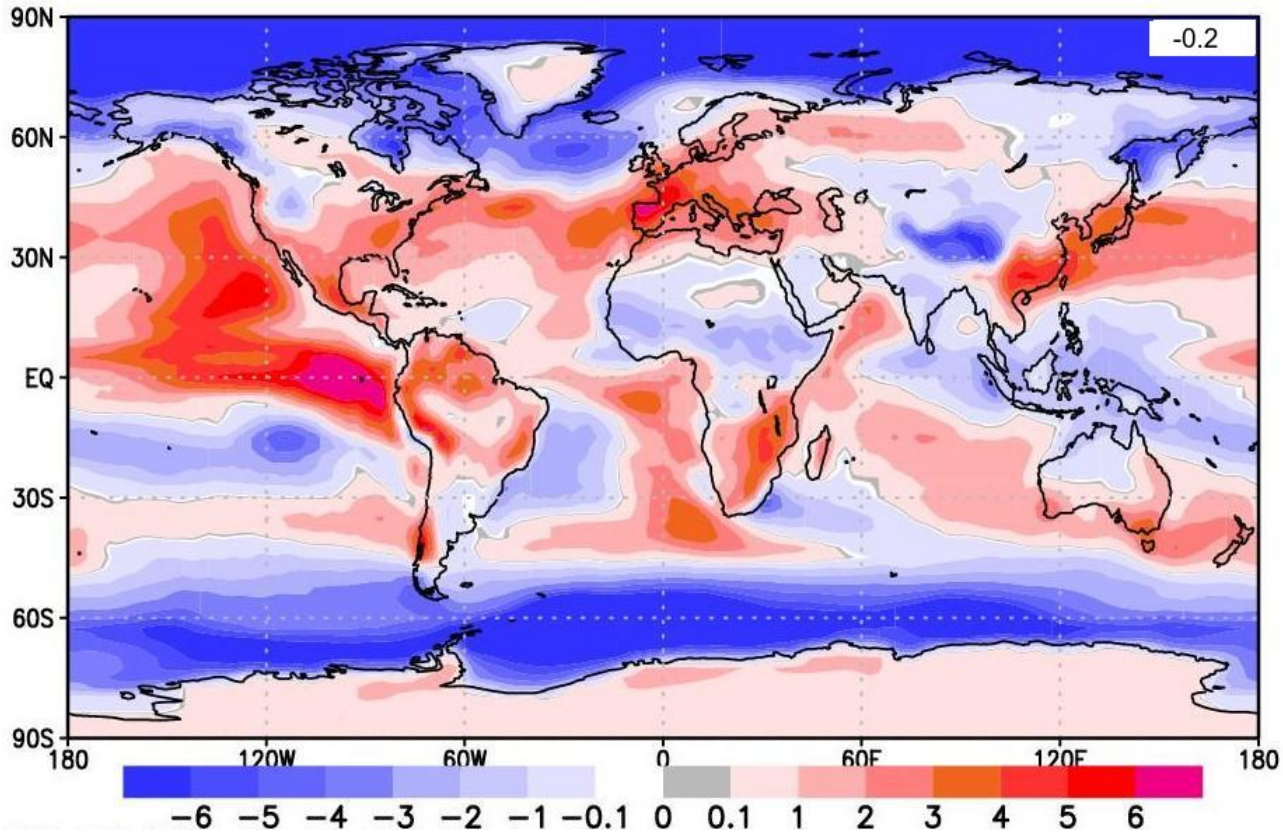

(c) Change in net cloud forcing.

Figure 13: Spatial distribution of the annual multimodel mean of change in a) SW cloud forcing, b) LW cloud forcing and c) net cloud forcing for 2071-2100 (compared to 1981-2010 base period). Units W/m^2.

5.4 Changes in the surface energy fluxes

5.4.1 Surface net radiation

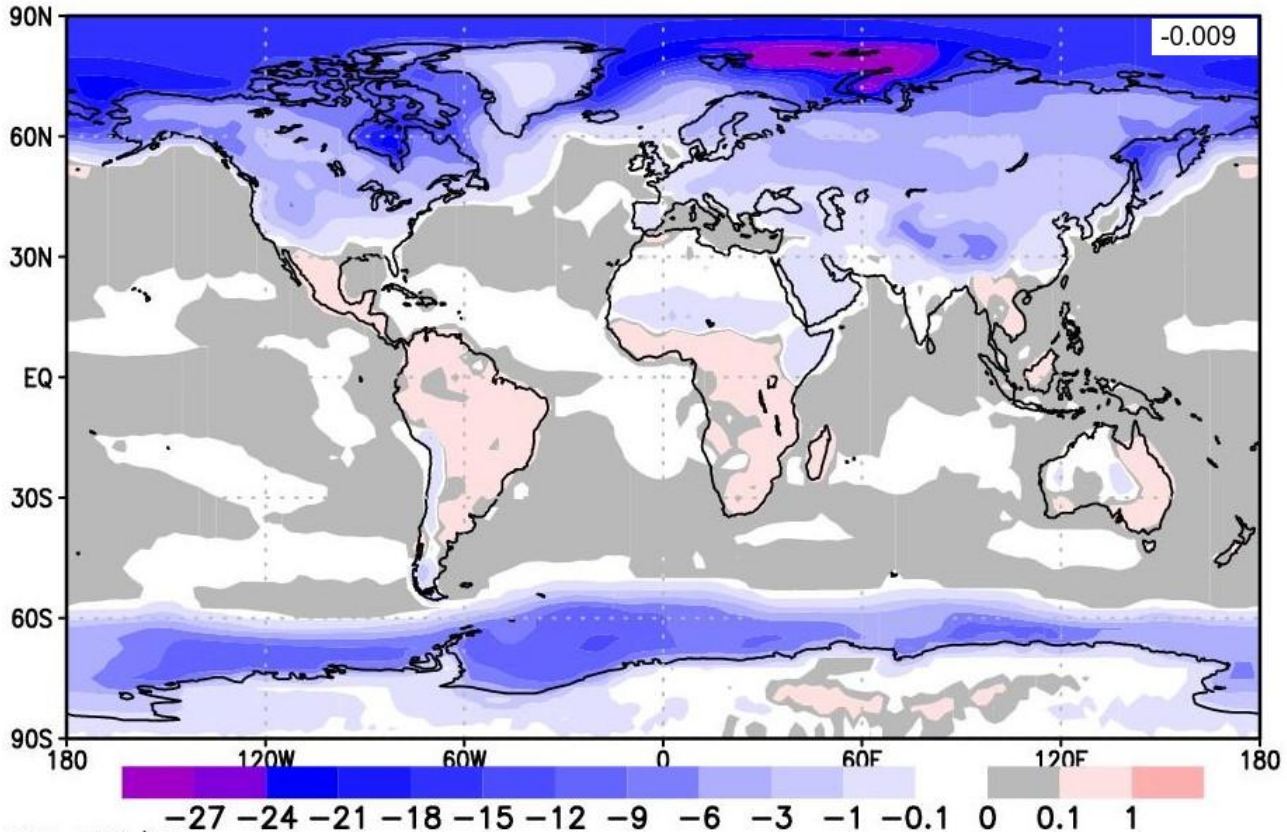

Figure 14: Spatial distribution of the annual multimodel mean of change in surface albedo for 2071-2100 (compared to 1981-2010 base period). Units %.

The changes in surface albedo ($\Delta\alpha$) are associated with changes in the $SW_{\uparrow}$ component and the projected warming. For instance, a decrease in α leads to reduced $SW_{\uparrow}$, and the warming is amplified. Figure 14 shows the spatial distribution of $\Delta\alpha$. The change is negligible over low-to-mid latitude oceans that are free of sea ice year round (both in present-day simulations and future projections). At higher latitudes, the decrease in sea ice cover and extent, due to warming, result in reduced surface albedo [Collins et al., 2013]. The magnitude of the change is largest in the Arctic latitudes and, as we noted in section 5.2, the projected warming is amplified by the snow/ice feedback (Fig. 10). Similarly, decreases in snow and frozen ground cover over the northern high latitude continents reduce α [Collins et al., 2013]. $\Delta\alpha$ is small over the Antarctic due to low temperatures and slow rate of melting of the ice sheet.

Moreover, changes in land cover patterns affect the surface albedo. Studies on the change in vegetation cover estimate that there is a net loss of forest cover in the tropics, for instance in the Amazon, while in the high latitudes there is increase in vegetation cover due to warming [Collins

et al., 2013,Falloon et al., 2012]. Over the northern high latitudes, increase in vegetation cover reduces α [Falloon et al., 2012] in addition to the snow/ice cover reductions. Figure 14 shows small increase in the surface albedo over the tropical forests. However, it is difficult to say whether the simulated change in α over these regions is due to changes in vegetation cover or if other factors affect the projected multimodel mean change. For example, the RCP8.5 scenario assumptions about the changes in land use patterns also affect $\Delta\alpha$.

The spatial distributions of the changes in all-sky and clear-sky components of the surface SW fluxes are depicted in Figure 15. The downward SW flux increases over areas of reduced cloud cover (Fig. 11), since direct reflection of SW radiation from clouds towards space is reduced, and correspondingly the downward SW radiation decreases over regions of increased cloud fraction, for instance in the northern polar regions (Fig. 15a). In addition to changes in cloud cover, the absorption of SW radiation in the atmosphere is enhanced by increased water vapor [Donohoe et al., 2014], and the clear-sky downward SW flux decreases in almost every region (Fig. 15c). Over continental Europe and eastern China, the $SW_{\downarrow cs}$ increases most likely due to assumed reductions in the anthropogenic emissions of air pollutants under RCP8.5 [Riahi et al., 2011].

The main contribution to $\Delta SW_{\uparrow}$ (Fig. 15b) and $\Delta SW_{\uparrow cs}$ (Fig. 15d) is the change in surface albedo, and in both cases the pattern of change is similar to that of Figure 14. For example, over the northern high latitudes and the southern high-latitude oceans, where the snow and sea ice cover is reduced and $|\Delta\alpha|$ is large, reflection from the surface decreases most. The slight differences between $\Delta SW_{\uparrow}$ and $\Delta SW_{\uparrow cs}$ are due to changes in cloudiness.

The spatial distribution of the change in (all-sky) net surface SW radiation is shown in Figure 15e. The positive values indicate increase in the radiation energy towards the surface and vice versa. In the low-to-mid latitudes, the effect of $\Delta SW_{\downarrow}$ dominates (Fig. 15a) but over the higher latitudes, the increase in radiation energy is due to changes in the surface albedo, and henceforth decrease in reflected SW radiation from the surface (Fig. 15b). On average, there is a small projected increase in the surface net SW radiation.

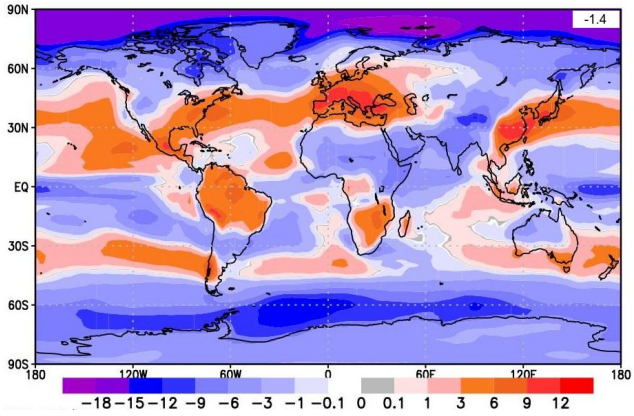

(a) $\Delta SW_{\downarrow}$.

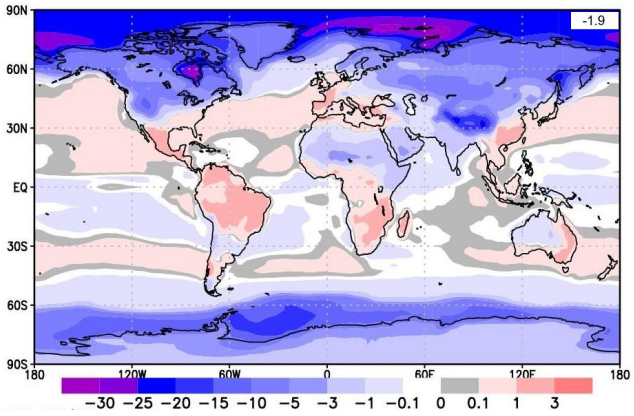

(b) $\Delta SW_{\uparrow}$.

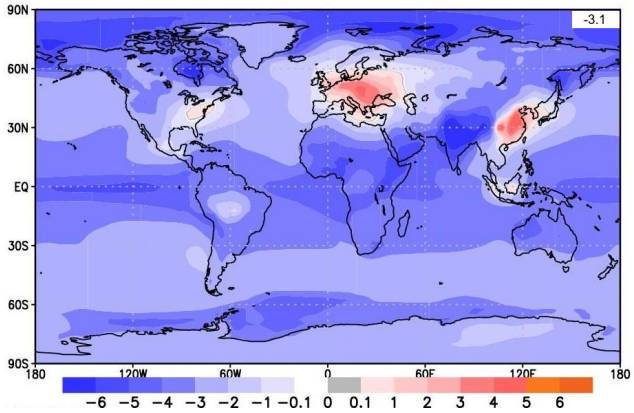

(c) $\Delta SW_{\downarrow cs}$.

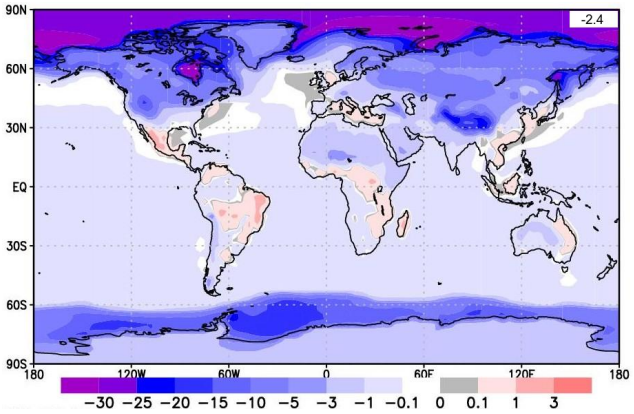

(d) $\Delta SW_{\uparrow cs}$.

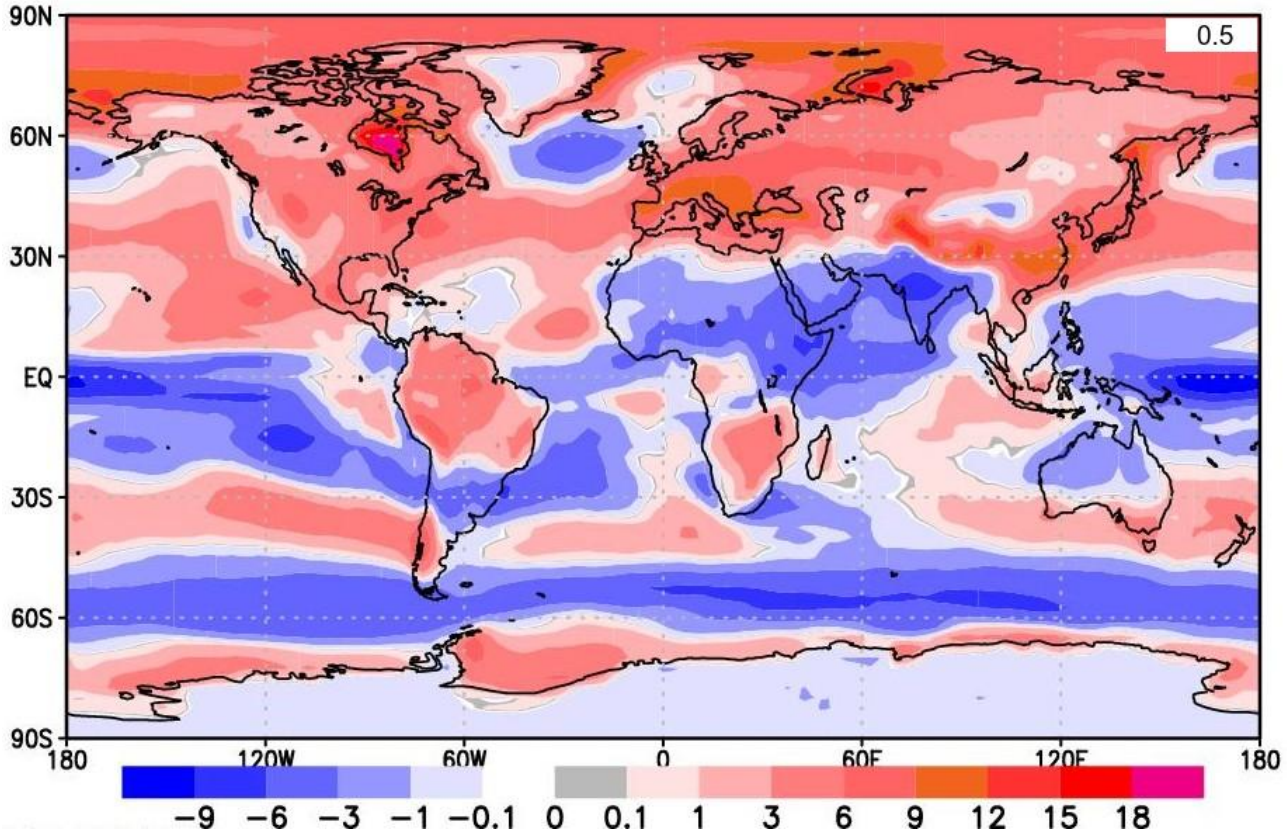

(e) The surface net SW radiation change.

Figure 15: Spatial distributions of the annual multimodel means of surface SW radiation changes for 2071-2100 (compared to 1981-2010 base period). Units W/m^2.

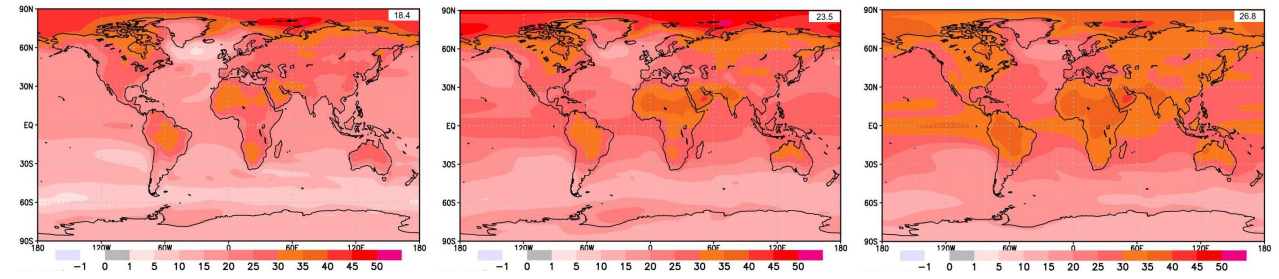

(a) $\Delta LW_{\uparrow}$ (b) $\Delta LW_{\downarrow}$ (c) $\Delta LW_{\downarrow cs}$

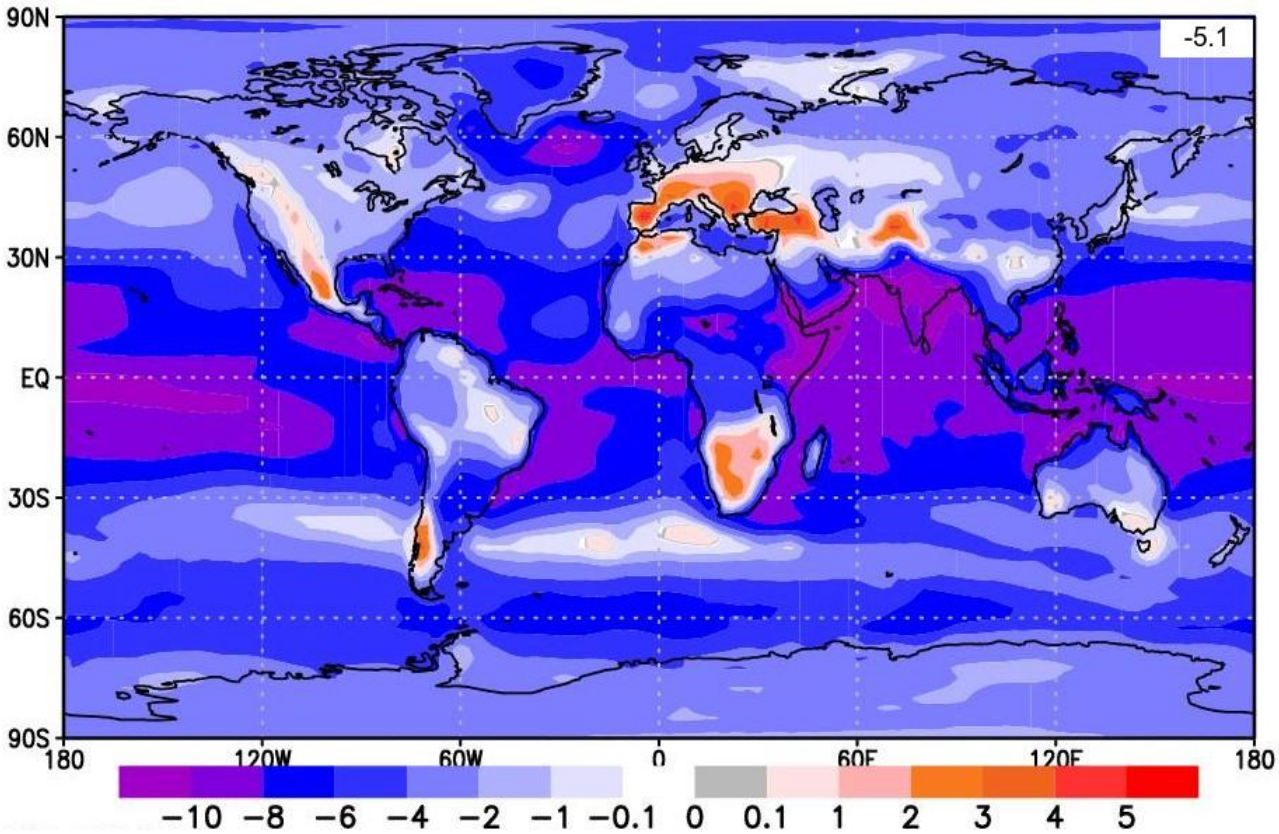

(d) The change in surface net LW radiation.

Figure 16: Spatial distribution of the annual multimodel mean of a) $\Delta LW_{\uparrow}$, b) $\Delta LW_{\downarrow}$, c) $\Delta LW_{\downarrow cs}$ and d) surface net LW radiation change (defined here as positive upward) for 2071-2100 (compared to 1981-2010 base period). Units W/m^2.

The spatial distributions of the changes in surface LW radiation fluxes are depicted in Figure 16. Since the magnitude of emitted LW radiation is directly proportional to the fourth power of the surface temperature, the pattern of change for $LW_{\uparrow}$ (Fig. 16a) is similar to that of ΔT (Fig. 10), and hence the emitted LW radiation from the surface increases. An important contribution to the changes in the atmospheric re-radiation components $LW_{\downarrow}$ (Fig. 16b) and $LW_{\downarrow cs}$ (Fig. 16c) is the increase in atmospheric GHGs, especially increase in atmospheric water vapor content. Additionally, most of the atmospheric re-radiation originates from the lower atmospheric layers, where the temperature change is closely similar to the pattern of surface

warming [Zhao et al., 1994]. For both the cloudy and cloud-free components of $LW_{\downarrow}$, the LW flux towards the surface increases. Due to the changes in cloud cover, there are some differences between $\Delta LW_{\downarrow}$ and $\Delta LW_{\downarrow cs}$, for instance in the northern polar regions where the cloud cover increases (Fig. 11) and $\Delta LW_{\downarrow} > \Delta LW_{\downarrow cs}$.

The change in surface net LW radiation is shown in Figure 16d, where the change is defined as positive upward. Over most areas, increase in atmospheric re-radiation (Fig. 16b) is larger than that in emitted LW radiation from the surface (Fig. 16a), and therefore the change in surface net LW flux is negative. Hence, mainly due to increases in atmospheric GHGs, the changes in surface LW fluxes result in amplified warming of the surface. The positive values, for instance over the Mediterranean region, are due to reduced cloud cover.

The spatial distribution of the change in surface net radiation (ΔR) is depicted in Figure 17. The change is positive over most areas, and the radiation energy at the surface increases. Part of this excess energy is divided between the turbulent heat fluxes, and part is stored in the oceans. The next section will study the changes in the surface energy budget.

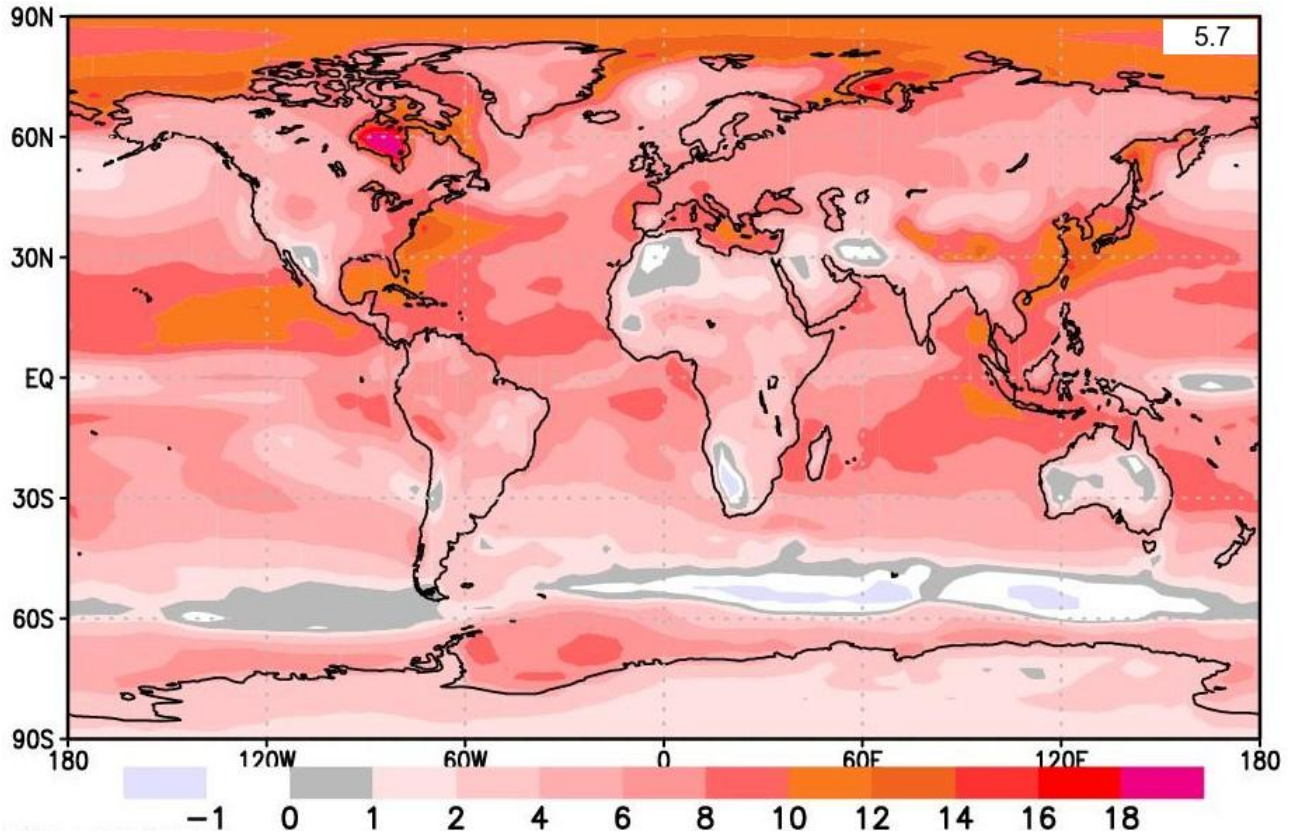

Figure 17: The spatial distribution of the annual multimodel mean of surface net radiation change (ΔR). Units W/m^2.

5.4.2 Turbulent heat fluxes and the surface energy budget

In the previous section we saw that the projected changes in the net surface radiation were positive in (almost) every region (Fig. 17). This surplus of radiation energy at the surface is further divided between the turbulent heat fluxes, and part is stored in the oceans or goes to horizontal energy transfer (Eq. 4). First, changes in the latent and sensible heat fluxes are studied.

The spatial distribution of the change in latent heat flux is depicted in Figure 18a. The main contributions to the pattern of change, in addition to increase in the net surface radiation, are the change in surface temperature and the soil moisture changes. Since there are many processes affecting the soil moisture content, future projections of the mean soil moisture change are relatively uncertain but multiple simulations (under RCP8.5) agree that soil moisture reductions in the Mediterranean region, the Southern Africa, northeast and southwest South America and southwestern USA are likely by the end of the 21st century [Collins et al., 2013]. Therefore, over these areas of reduced soil moisture, $LE_{\uparrow}$ decreases (Fig. 18a).

Except for areas with decreasing soil moisture, the change in latent heat flux is, on average, positive. In Greenland and over the Antarctic ice sheet, the change is small but over most of the other continental regions, $LE_{\uparrow}$ increases due to increase in the net surface radiation and the warming (the Clasius-Clapeyron relation). Similarly, over the low-to-mid latitude oceans and the northern polar region, $LE_{\uparrow}$ increases.

The spatial distribution of the change in sensible heat flux is shown in Figure 18b. We first note that over the low-to-mid latitude continents, $H_{\uparrow}$ increases in the regions of reduced $LE_{\uparrow}$, since ΔR is positive. Over the low-to-mid latitude oceans, $H_{\uparrow}$ is slightly decreasing due to increases in the latent heat flux.

The magnitude of the change in sensible heat flux depends partly on the temperature difference between the surface and the above atmosphere, as mentioned in Chapter 4.3.2. Over some ocean regions, for instance in the northern North Atlantic, $H_{\uparrow}$ decreases due to warming. Similarly, $\Delta LE_{\uparrow}$ is negative, and $\Delta(R - H_{\uparrow} - LE_{\uparrow})$ (Fig. 18c) is positive. Hence, the heat transfer from the ocean to the atmosphere decreases, for example over the northern North Atlantic. If we compare the results between Figure 9 and Figure 18c, we notice that the heat exchange between the ocean surface and the atmosphere declines nearly everywhere over the low-to-mid latitude oceans. Moreover, $\Delta(R - H_{\uparrow} - LE_{\uparrow})$ is negligible over the continents.

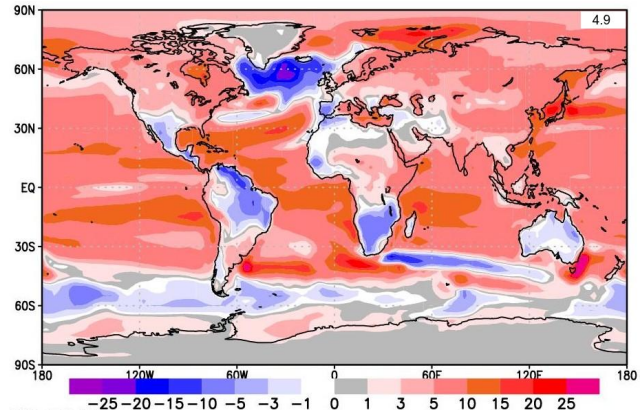

(a) $\Delta LE_{\uparrow}$

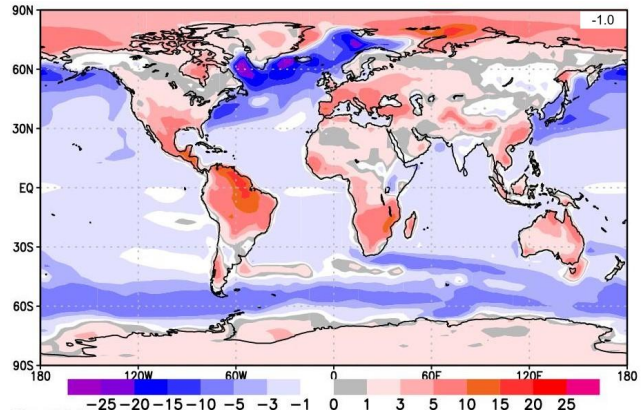

(b) $\Delta H_{\uparrow}$

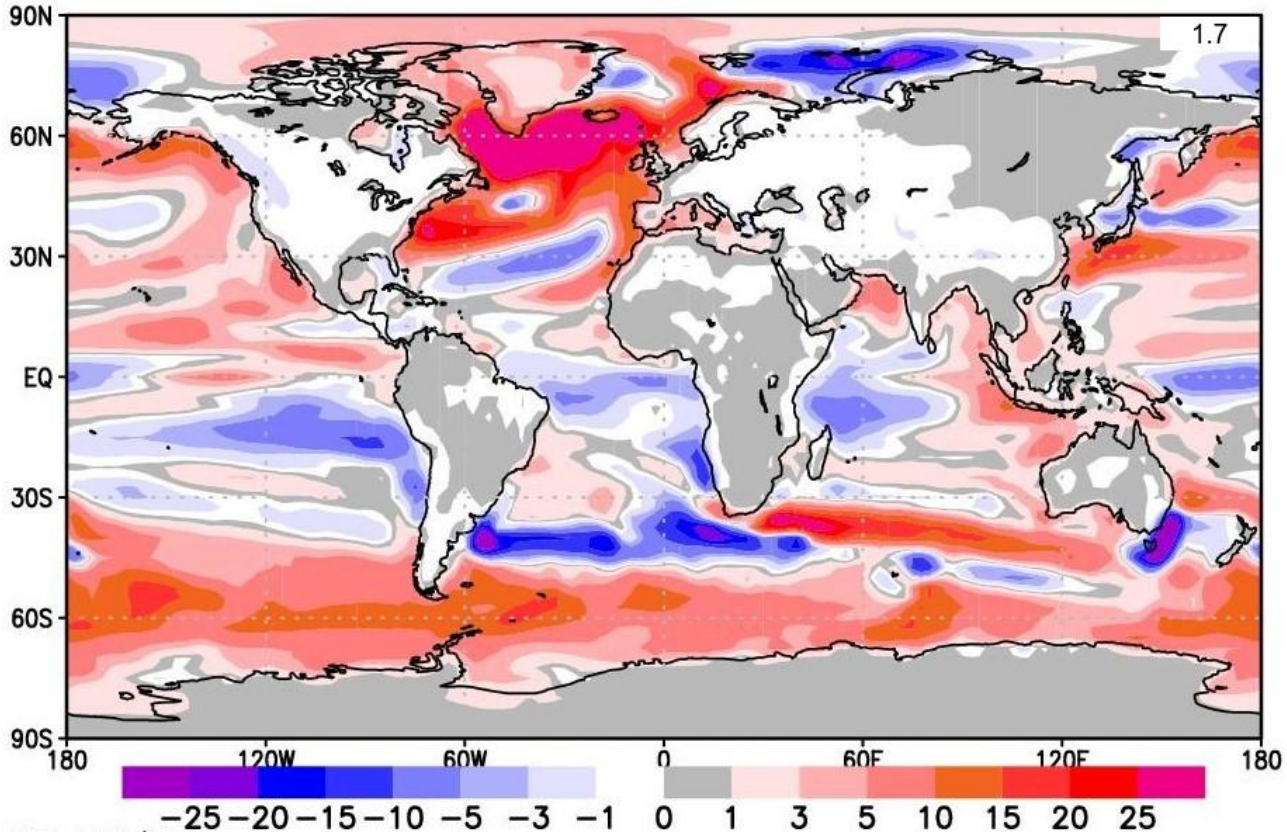

(c) $\Delta(R - H_{\uparrow} - LE_{\uparrow})$

Figure 18: The spatial distribution of the annual multimodel mean of change in a) latent heat flux, b) sensible heat flux and c) $R - H_{\uparrow} - LE_{\uparrow}$. Units W/m^2.

While this chapter presented the multimodel mean changes of the components of the energy budget, surface temperature and clouds, the next chapter will study the model-to-model consistency of the simulated changes. In addition to examining the differences and the similarities between the simulations, the next chapter also gives insight to how the energy budget components are related to the change in surface temperature.

6 Intermodel consistency of the simulated changes

This chapter studies the intermodel consistency of the simulated changes in Chapter 5. Climate model projections of future changes are uncertain in the sense that, while they help us to understand the possible climate change, they cannot present a truly accurate prediction of the future state of our complex climate system, for instance due to various technical reasons and uncertainty due to scenario choices in climate modelling [Collins et al., 2013]. In this thesis, the future projections presented in the previous chapter were multimodel means, and hence the intermodel differences and model agreement must be studied in order to attain better confidence in the results.

Component	SD	Units (SD)	CORR
ΔT	0.7	K	1.0
$\Delta SW_{\downarrow TOA}$	0.06	W/m^2	0.2
$\Delta SW_{\uparrow TOA}$	2.2	W/m^2	-0.53
$\Delta LW_{\uparrow TOA}$	2.0	W/m^2	0.53
$\Delta SW_{\downarrow}$	1.4	W/m^2	0.13
$\Delta SW_{\uparrow}$	0.8	W/m^2	0.05
$\Delta LW_{\downarrow}$	4.5	W/m^2	0.89
$\Delta LW_{\uparrow}$	4.0	W/m^2	0.98
$\Delta H_{\uparrow}$	0.4	W/m^2	-0.004
$\Delta LE_{\uparrow}$	1.3	W/m^2	0.35
$\Delta SW_{\uparrow TOA,cs}$	1.2	W/m^2	-0.44
$\Delta LW_{\uparrow TOA,cs}$	1.6	W/m^2	0.8
$\Delta SW_{\downarrow cs}$	1.3	W/m^2	-0.64
$\Delta SW_{\uparrow cs}$	0.9	W/m^2	-0.43
$\Delta LW_{\downarrow cs}$	5.3	W/m^2	0.96
ΔCLT	1.4	%	-0.27

Table 4: The rounded globally and annually averaged values for the study of intermodel consistency. The second column: the intermodel standard deviations (SD) of the global mean change in the 16 variables. The third column: the global area means (from Fig. 21) for the intermodel correlations (CORR) between ΔT and the change in each variable.

First, the differences between the model projections are studied with the intermodel standard deviations of the changes in the 16 variables. Then, the regional intermodel agreement on the changes is examined with the spatial distributions of the ratio of multimodel mean to the intermodel standard deviation. Lastly, the intermodel correlations between ΔT and each individual variable are discussed. The global area means for the standard deviations of the changes and the intermodel correlations are listed in Table 4. We note that $\Delta SW_{\downarrow TOA}$ is once again negligible, and the global mean correlation between the surface LW radiation fluxes and ΔT is strongly positive.

6.1 Intermodel standard deviations

The spatial distributions of intermodel standard deviations for the annual mean change in each of the 15 variables are depicted in Figure 19. The intermodel variation in the projections is, among other factors and choices in climate modelling, due to differences in simulated cloud fraction, snow and ice cover and atmospheric water vapor content. The intermodel standard deviation for $\Delta SW_{\downarrow TOA}$ is not studied here, since the change in it was negligible.

We first note that the intermodel differences for ΔT are large in the northern high latitudes and over the Southern oceans (Fig. 19a), where the change in surface temperature is also large (Fig. 10). As discussed in Chapter 5.2, there are various physical processes affecting the pattern of surface warming, for instance changes in the snow/ice cover over the high latitudes. Hence, even though climate models agree on amplified surface warming over the northern polar regions, the magnitude of the change varies between the models [Collins et al., 2013]. Furthermore, the intermodel differences are smaller over the low-to-mid latitudes and the Antarctica (Fig. 19a).

For the change in cloud cover, the intermodel standard deviation is large especially over the northern high latitudes, relatively large over parts of the low-to-mid latitude oceans (for instance the Eastern Pacific) and somewhat large over the Southern ocean (Fig. 19d). The change in cloud cover was also large (Fig. 11) in these regions. The intermodel differences in ΔCLT are most likely due to uncertainty in the simulation of clouds, since parametrization of several small-scale processes is needed in the simulation of clouds [Boucher et al., 2013].

For the TOA radiation fluxes, the standard deviations of $\Delta SW_{\uparrow TOA}$ (Fig. 19b) and $\Delta LW_{\uparrow TOA}$ (Fig. 19c) are both amplified over the low-to-mid latitude oceans, presumably due to differences in ΔCLT. Therefore, the spatial distribution of intermodel standard deviation of $\Delta SW_{\uparrow TOA,cs}$ (Fig. 19e) approaches that of ΔT more clearly, since the intermodel differences in $\Delta SW_{\uparrow TOA,cs}$ are notably larger over the high latitudes. Over the high latitudes, the standard deviation

reflects the intermodel differences in projected snow and sea ice cover change that reduces the reflected SW flux from the surface [Collins et al., 2013]. Similarly, the standard deviation of $\Delta LW_{\uparrow TOA,cs}$ (Fig. 19f) is slightly larger over the same regions, but the intermodel spread is not as considerable as that of $\Delta SW_{\uparrow TOA,cs}$.

The standard deviation of $\Delta SW_{\downarrow}$ (Fig. 19g) is similar to that of $\Delta SW_{\uparrow TOA}$, while the intermodel variation in $\Delta SW_{\downarrow cs}$ (Fig. 19j) is minute compared to differences in other radiation fluxes. The standard deviations of $\Delta SW_{\uparrow}$ (Fig. 19h) and $\Delta SW_{\uparrow cs}$ (Fig. 19k) are amplified over the high latitudes, similar to differences in $\Delta SW_{\uparrow TOA,cs}$, and the intermodel variation is small over the low-to-mid latitude oceans, where $\Delta SW_{\uparrow}$ (Fig. 15b) and $\Delta SW_{\uparrow cs}$ (Fig. 15d) are both small and the average change in surface albedo is negligible (Fig. 14).

The standard deviations of the surface LW fluxes are relatively large, and the difference is amplified over the high latitudes and parts of the low-to-mid latitude oceans. The intermodel standard deviation of $\Delta LW_{\uparrow}$ (Fig. 19o) approaches in pattern that of ΔT, not surprisingly giving the dependence of thermal radiation on the surface temperature. The intermodel variations in $\Delta LW_{\downarrow}$ (Fig. 19i) and $\Delta LW_{\downarrow cs}$ (Fig. 19l) are large, probably due to intermodel differences in projections of water vapor increase with surface warming [Räisänen, 2016]. Additionally, most of the atmospheric re-radiation originates from the lower atmospheric layers where the temperature change is approximately similar to the surface [Zhao et al., 1994]. Hence, the intermodel differences in ΔT affect the standard deviations of the atmospheric re-radiation components.

The intermodel differences in $\Delta H_{\uparrow}$ (Fig. 19m) are larger over the high latitudes and the continents, and small over the low-to-mid latitude oceans, Greenland and the Antarctica. The standard deviation of $\Delta LE_{\uparrow}$ (Fig. 19n) is small over Greenland and the Antarctica, but larger over other areas. For both of the turbulent heat fluxes, the intermodel differences are amplified over the northern North Atlantic, where the magnitude of change was large (Fig. 18a,b). This could be due to model-to-model differences in the projected changes in ocean circulation and sea ice cover [Räisänen, 2016]. Over land, $\Delta LE_{\uparrow}$ is partly affected by the change in surface soil moisture content but intermodel agreement on the projections of the soil moisture change is difficult to attain due to the multitude of physical processes included [Collins et al., 2013], which could explain some of the intermodel variation in $\Delta LE_{\uparrow}$, and consequently $\Delta H_{\uparrow}$.

In conclusion, the largest intermodel variations occur over the high latitudes, presumably due to the differences in the simulated snow and sea ice cover changes. For the all-sky radiation fluxes, cloud cover projections affect the standard deviations, especially over the low-to-mid latitudes. Since the water vapor feedback depends on the change in surface temperature, it amplifies the differences in $\Delta LW_{\downarrow}$ and $\Delta LW_{\downarrow cs}$ between models with different projections of

the warming.

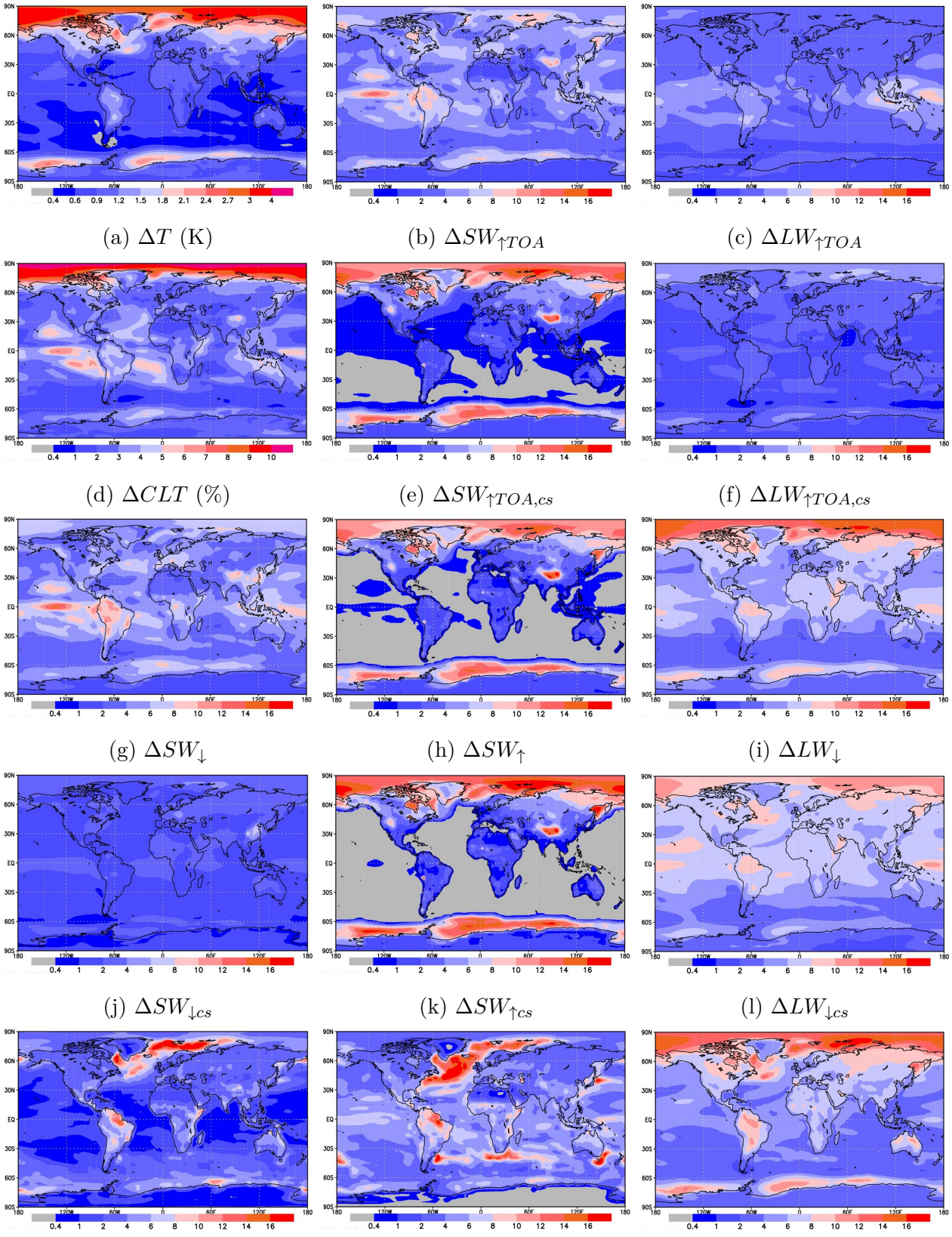

(a) ΔT (K) (b) $\Delta SW_{\uparrow TOA}$ (c) $\Delta LW_{\uparrow TOA}$

(d) ΔCLT (%) (e) $\Delta SW_{\uparrow TOA,cs}$ (f) $\Delta LW_{\uparrow TOA,cs}$

(g) $\Delta SW_{\downarrow}$ (h) $\Delta SW_{\uparrow}$ (i) $\Delta LW_{\downarrow}$

(j) $\Delta SW_{\downarrow cs}$ (k) $\Delta SW_{\uparrow cs}$ (l) $\Delta LW_{\downarrow cs}$

(m) $\Delta H_{\uparrow}$ (n) $\Delta LE_{\uparrow}$ (o) $\Delta LW_{\uparrow}$

Figure 19: The spatial distributions of the intermodel standard deviations of the change in studied variables a-o. Units W/m^2, unless stated otherwise.

6.2 Intermodel agreement on the projected changes

In this section, the agreement among models is studied briefly with the ratio of the multimodel mean to the intermodel standard deviation. The spatial distributions are depicted in Figure 20, where the regions with highest/lowest magnitudes indicate stronger consistency in projections across the models. Again, $\Delta SW_{\downarrow TOA}$ is not studied here. We first note that for ΔT (Fig. 20a), $\Delta LW_{\downarrow}$ (Fig. 20i), $\Delta LW_{\downarrow cs}$ (Fig. 20l) and $\Delta LW_{\uparrow}$ (Fig. 20o), the models show strong agreement on the sign and magnitude of the change in every region, specifically over the low-to-mid latitudes, Greenland and the Antarctica.

The models tend to agree on cloud cover projections mostly over the mid-latitudes, while the consistency is less strong over the higher latitudes and weak in parts of the low-to-mid latitudes, especially around the equator (Fig. 20d). Figures 20c and 20f show weaker agreement on the projections of TOA LW fluxes over parts of the low-to-mid latitudes, but the multimodel mean change in all-sky OLR (Fig. 12b) was also small in these regions. Interestingly, the models show relatively significant agreement on the sign of projected changes in cloud-free SW radiation fluxes (Fig. 20e, 20j and 20k), which were decreasing. Since changes in cloud cover affect the other SW radiation components (Fig. 20b, 20g and 20h), the model agreement is weaker over parts of the low-to-mid latitudes but the models show consistency in projected changes over other regions. Additionally, the models tend to agree on the sign and magnitude of turbulent heat flux projections (Fig. 20m and 20n), especially over the oceans and higher latitudes.

In conclusion, the models tend to agree strongly on the projections ΔT and the surface LW fluxes, while the consistency in cloud-free SW flux changes across the models is also significant. In the previous section, the standard deviations of the changes showed the magnitude of regional intermodel differences of the projections, and this section examined agreement of the models on the direction of the projected changes. The next section studies the intermodel correlation between ΔT and other components, which helps us better identify the relationship between these variables.

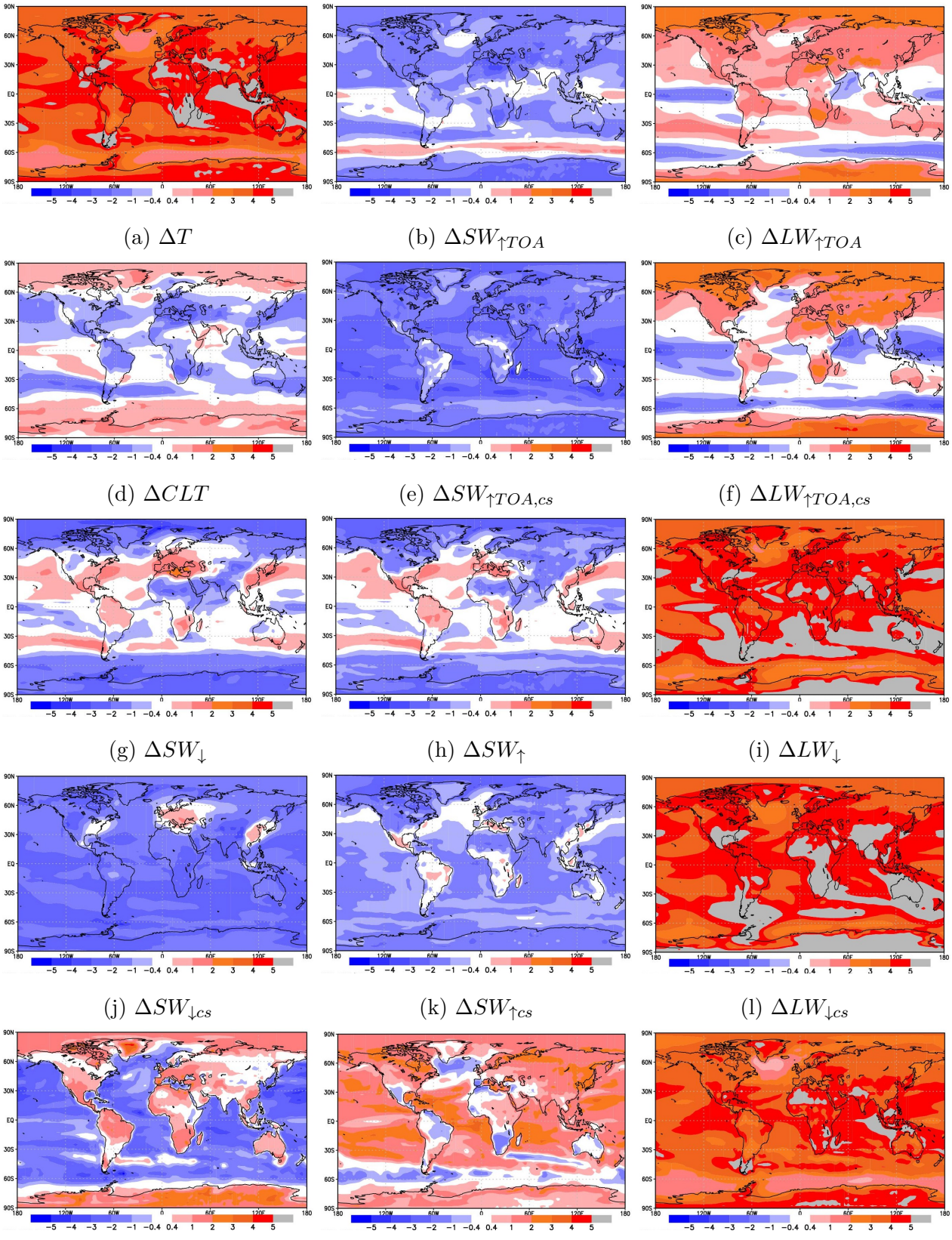

(a) ΔT (b) $\Delta SW_{\uparrow TOA}$ (c) $\Delta LW_{\uparrow TOA}$

(d) ΔCLT (e) $\Delta SW_{\uparrow TOA,cs}$ (f) $\Delta LW_{\uparrow TOA,cs}$

(g) $\Delta SW_{\downarrow}$ (h) $\Delta SW_{\uparrow}$ (i) $\Delta LW_{\downarrow}$

(j) $\Delta SW_{\downarrow cs}$ (k) $\Delta SW_{\uparrow cs}$ (l) $\Delta LW_{\downarrow cs}$

(m) $\Delta H_{\uparrow}$ (n) $\Delta LE_{\uparrow}$ (o) $\Delta LW_{\uparrow}$

Figure 20: The spatial distributions depicting the intermodel agreement (mean/standard deviation) of the change in studied variables a-o.

6.3 Intermodel correlations

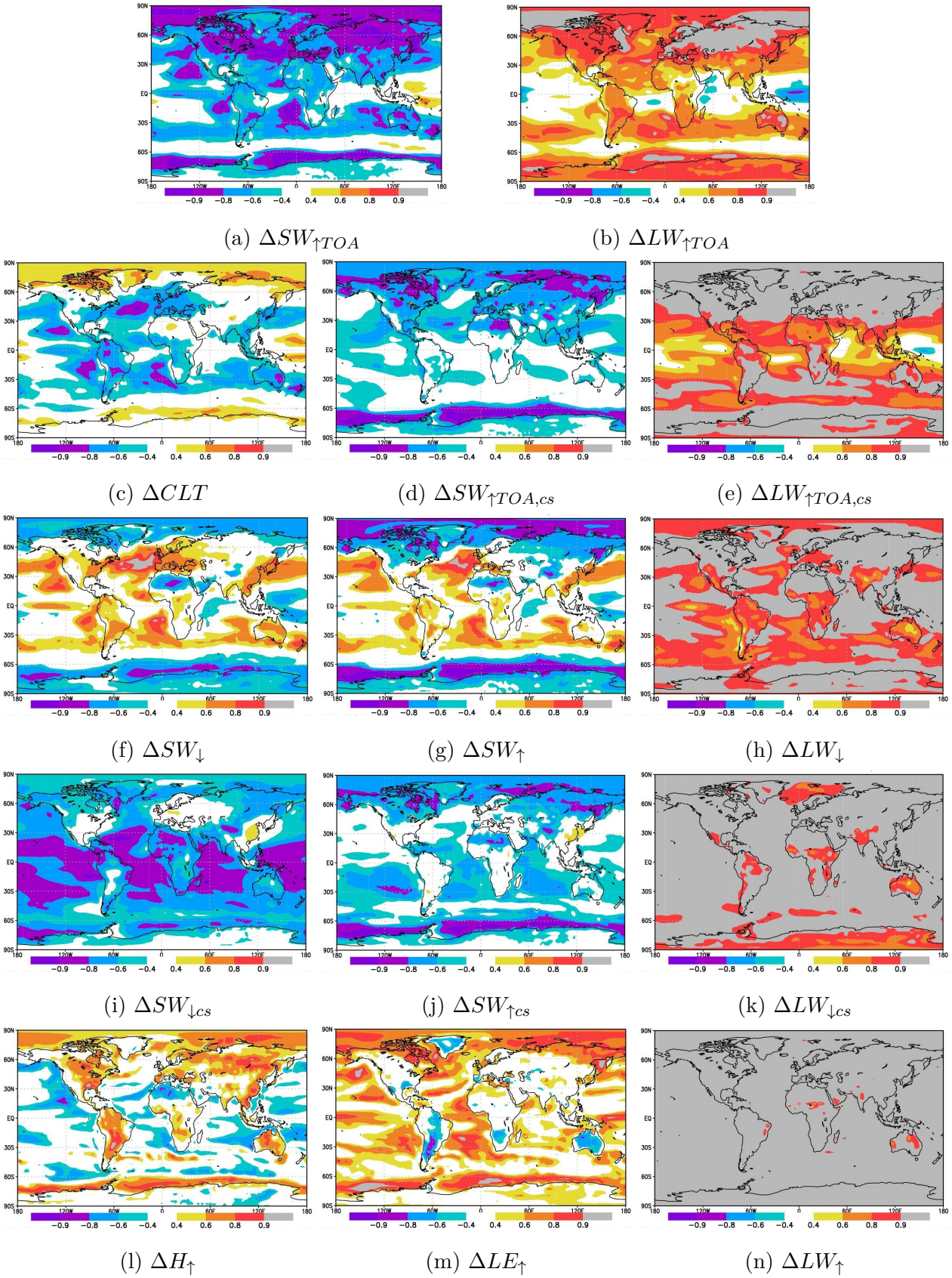

(a) $\Delta SW_{\uparrow TOA}$ (b) $\Delta LW_{\uparrow TOA}$

(c) ΔCLT (d) $\Delta SW_{\uparrow TOA,cs}$ (e) $\Delta LW_{\uparrow TOA,cs}$

(f) $\Delta SW_{\downarrow}$ (g) $\Delta SW_{\uparrow}$ (h) $\Delta LW_{\downarrow}$

(i) $\Delta SW_{\downarrow cs}$ (j) $\Delta SW_{\uparrow cs}$ (k) $\Delta LW_{\downarrow cs}$

(l) $\Delta H_{\uparrow}$ (m) $\Delta LE_{\uparrow}$ (n) $\Delta LW_{\uparrow}$

Figure 21: The spatial distributions of the intermodel correlations between ΔT and the variable specified below the figure.

The spatial distributions of the intermodel correlations between ΔT and each individual variable are studied in Figure 21. In general, a stronger positive (negative) correlation with ΔT reflects that models with enhanced warming also project larger increases (decreases) in the studied variable. Again, the correlation between $\Delta SW_{\downarrow TOA}$ and ΔT was negligible, and therefore it is not studied here.

We first note that there is a strong positive intermodel correlation between the changes in LW fluxes and ΔT. At the top of the atmosphere, the correlation is high over the mid-to-high latitudes, and small over lower latitude oceans and parts of the mid-latitude Southern oceans (Fig. 21b). However, the correlation between $\Delta LW_{\uparrow TOA,cs}$ and ΔT is strongly positive almost everywhere (Fig. 21e). For the surface LW fluxes, there is a strong positive intermodel correlation in every region, especially with $\Delta LW_{\uparrow}$ which is, as mentioned before, directly proportional to the fourth power of the surface temperature (Fig. 21n). In models with larger ΔT, the atmospheric water vapor content increases more and the greenhouse effect is stronger, which partly explains the strong positive correlation between $\Delta LW_{\downarrow}$ (Fig. 21h) or $\Delta LW_{\downarrow cs}$ (Fig. 21k) and ΔT [Räisänen, 2016]. Furthermore, the warming of the lower atmospheric layers is also larger in models with larger surface warming, and most of the atmospheric re-radiation occurs from there [Zhao et al., 1994].

At the top of the atmosphere, the correlation between $\Delta SW_{\uparrow TOA}$ and ΔT is strongly negative over the high latitudes and parts of the mid-latitude oceans (Fig. 21a). The intermodel correlation between $\Delta SW_{\uparrow TOA,cs}$ and ΔT is less strong over the high northern latitudes, and relatively weak over the mid-latitudes (Fig. 21d). Over the high latitudes, the negative correlations in both cases reflect the reduced snow and sea ice cover with larger warming [Räisänen, 2016]. The difference in Figures 21a and 21d is most likely explained by the changes in cloud cover, since we note that ΔCLT correlates positively with ΔT over the high latitudes (Fig. 21c), where the correlation between $\Delta SW_{\uparrow TOA}$ and the change in temperature was stronger compared to $\Delta SW_{\uparrow TOA,cs}$. $\Delta SW_{\uparrow}$ (Fig. 21g) and $\Delta SW_{\uparrow cs}$ (Fig. 21j) correlate negatively with ΔT over the high latitudes, where the intermodel standard deviations were also larger (Fig. 19). Significantly, there is a substantial negative correlation between $\Delta SW_{\downarrow cs}$ and ΔT over the low-to-mid latitude oceans (Fig. 21i), which is most likely caused by increase in atmospheric water vapor content in models with larger surface warming [Donohoe et al., 2014].

The intermodel correlation between ΔCLT and ΔT is negative over parts of the mid-latitude oceans, positive over the Arctic Sea and the Southern oceans (possibly due to the reduced ice cover), and relatively small in other areas (Fig. 21c). Additionally, there is a positive correlation between $\Delta H_{\uparrow}$ and ΔT over some land areas and the high-latitude oceans (Fig. 21l)

and a stronger positive correlation between $\Delta LE_{\uparrow}$ and ΔT over the high-latitude oceans and parts of the low-to-mid latitude oceans (Fig. 21m). However, the strong correlations between the changes in SW and LW fluxes and ΔT, presumably due to snow/ice cover reductions and increases in atmospheric water vapor, reflect that in most part the radiation fluxes (not including $LW_{\uparrow}$) amplify the intermodel differences in the projections of surface warming.

7 Conclusions

In this thesis, the present-day distributions and the future projections of changes in TOA radiation fluxes and surface energy budget in 23 CMIP5 models were studied, with the baseline period of 1981-2010 and the comparison scenario period of 2071-2100 (RCP8.5). Altogether 16 variables, including all-sky and clear-sky components of the radiation fluxes, turbulent heat fluxes, cloud cover and near-surface temperature, were chosen to be examined, and the results were presented as multimodel means. Additionally, the intermodel consistency of the simulated changes was studied with the intermodel standard deviations and the ratio of multimodel mean to the intermodel standard deviation. Furthermore, the correlation between ΔT and each individual variable was discussed.

The positive energy imbalance at the top of the atmosphere, due to some external factor (natural or anthropogenic), and the resulting accumulation of energy in the climate system leads to warming of the surface and the lower atmospheric layers. Various feedbacks associated with, for instance, changes in cloud cover, atmospheric water vapor content or the change in ice/snow cover affect ΔT by altering the fluxes of energy that modify the pattern of surface warming. The geographical distributions of changes in Chapter 5 as well as the intermodel correlations in Chapter 6.3 give insight to the contribution of each energy balance component to the near-surface temperature change.

We found that **the global average temperature change**, according to the simulations, is 3.5 K. ΔT is positive in every region (Fig. 10), and the change is largest in the northern high latitudes where ΔT is amplified by the snow/ice feedback [Holland and Bitz, 2003, Collins et al., 2013]. The intermodel differences for ΔT are also amplified over the Arctic (Fig. 19a): while the models generally agree on larger ΔT over the northern polar regions, the magnitude of the warming varies between the simulations [Collins et al., 2013]. In addition, the simulated warming is larger over land compared to oceans due to oceans' higher heat capacity, increase in latent heat flux over the sea surface and reduced soil moisture in drying land areas (decrease in evaporation) [Collins et al., 2013]. The sea surface temperature change is smallest over North

Atlantic and the Southern oceans, and largest in the Tropical Pacific.

The global average net radiation change at the TOA is 1.9 W/m^2, and hence the energy imbalance increases compared to the present-day value 0.9 W/m^2 from Table 3, or the estimate from Chapter 2.1 (0.6 W/m^2 [Hansen et al., 2011]). On average, **OLR** increases due to the simulated warming of the surface and the atmosphere. The change is modest compared to the surface LW fluxes due to absorption of thermal radiation by increased GHGs in the atmosphere and the effect of clouds, the latter explaining partly the geograpical variations in $\Delta LW_{\uparrow TOA}$ (Fig. 12b) and the amplified intermodel differences over the low-to-mid latitude oceans for all-sky OLR (Fig. 19c). The intermodel correlation between ΔT and $\Delta LW_{\uparrow TOA}$ (Fig. 21b) is high elsewhere but small over lower latitude oceans and parts of the mid-latitude Southern oceans, presumably due to clouds, while the correlation between ΔT and $\Delta LW_{\uparrow TOA,cs}$ (Fig. 21e) is strongly positive in almost every region, as expected given the temperature dependence of LW flux magnitude.

For the TOA SW fluxes, the global mean change is negative and the reflection of incident SW radiation is reduced due to absorption by increased water vapor in the atmosphere and reduced surface albedo over high latitudes [Donohoe et al., 2014]. In other words, we found that the TOA energy imbalance is enhanced not only by increase in OLR but also due to increase in absorption of SW radiation, which further adds to the warming. The geographical distribution of the net TOA SW radiation change (Fig. 12a) is affected by the changes in sea ice and snow cover in the high latitudes, and additionally changes in cloud cover affect $\Delta SW_{\uparrow TOA}$ through reducing or increasing the reflection from clouds. The intermodel differences in $\Delta SW_{\uparrow TOA}$ (Fig. 19b) are amplified over low-to-mid latitude oceans due to variations in cloud cover projections (Fig. 19d), while the standard deviation of $\Delta SW_{\uparrow TOA,cs}$ (Fig. 19e) is larger over the high latitudes reflecting the intermodel spread in projected ice and snow cover changes between the models. The strongly negative correlation between $\Delta SW_{\uparrow TOA}$ and ΔT (Fig. 21a) over the high latitudes and parts of the low-to-mid latitude oceans along with the negative correlation between $\Delta SW_{\uparrow TOA,cs}$ and ΔT (Fig. 21d) over the high latitude oceans also reflect the changes in cloud cover and the reduced sea ice and snow cover with larger warming, respectively.

The global averages for **the projected changes in surface SW fluxes** are all negative. The clear-sky downward SW flux (Fig. 15c) decreases in most regions due to enhanced absorption of SW radiation by increase in atmospheric water vapor content [Donohoe et al., 2014]. The geographical distribution for the all-sky downward SW flux (Fig. 15a) differs from $\Delta SW_{\downarrow cs}$ due to changes in cloud cover and reflection from clouds. The intermodel variation in $\Delta SW_{\downarrow}$ (Fig. 19g) is similar to $\Delta SW_{\uparrow TOA}$, while the standard deviation for $\Delta SW_{\downarrow cs}$ (Fig. 19j) is small

and the models agree relatively strongly on the sign of the projected change (Fig. 20j). There is a strong negative correlation between $\Delta SW_{\downarrow cs}$ and ΔT (Fig. 21i)over the mid-latitude oceans, further suggesting that the absorption of SW radiation is enhanced in models with larger warming. For the upward SW fluxes (Fig. 15b, Fig. 15d), the changes in surface albedo (Fig. 14) affect mostly the patterns of change, especially over the high latitudes where the sea ice and snow cover are reduced due to the warming and the reflection of SW radiation decreases, the intermodel standard deviations are larger (Fig. 19h, Fig. 19k) and the correlations with ΔT are negative (Fig. 21g, Fig. 21j). On average, the net SW radiation towards the surface is projected to increase slightly (Fig. 15e).

As was expected, **the projected changes in surface LW fluxes** are large with $\Delta LW_{\downarrow}$ (Fig. 16b) and $\Delta LW_{\downarrow cs}$ (Fig. 16c) increasing even more than $\Delta LW_{\uparrow}$ (Fig. 16a), and hence the surface warming is amplified. The models agree strongly on the projected changes (Fig. 20i, 20l, 20o) and the correlation between the changes in surface LW fluxes and ΔT is strongly positive in every region (Fig. 21h, 21k, 21n). The patterns of change for the surface LW fluxes follow that of the surface temperature, since thermal radiation is directly proportional to T^4 and the temperature change in the lower atmospheric layers (where most of the atmospheric re-radiation originates from) is closely similar to ΔT at the surface [Zhao et al., 1994], partly explaining the strong positive correlations. The enhanced greenhouse effect plays also a major role in the projected change for the atmospheric re-radiation components, with stronger absorption and emissions of the thermal radiation due to increase in GHGs, mainly water vapor.

The change in surface net radiation is positive in almost every area (Fig. 17), and part of this excess energy is divided between $LE_{\uparrow}$ and $H_{\uparrow}$, while part goes to ocean heat storage and to horizontal energy transfer. $LE_{\uparrow}$ decreases over areas of reduced soil moisture but, on average $\Delta LE_{\uparrow}$ is positive reflecting stronger evaporation with the simulated warming (Fig. 18a). Over the high-latitude oceans and parts of the low-to-mid latitude oceans, there is a relatively strong positive correlation between $\Delta LE_{\uparrow}$ and ΔT (Fig. 21m). Since the change in soil moisture content affects $\Delta LE_{\uparrow}$ (along with ΔT), the standard deviation of $\Delta LE_{\uparrow}$ (Fig. 19n) over land is partly explained by the intermodel variations in simulating the soil moisture change [Collins et al., 2013]. Over land, $\Delta H_{\uparrow}$ increases in the regions of reduced $LE_{\uparrow}$ and over low-to-mid latitude oceans $H_{\uparrow}$ is decreasing slightly due to increase in $LE_{\uparrow}$ (Fig. 18b). The change in both turbulent heat fluxes is strongly negative over the northern North Atlantic, where the intermodel differences for $\Delta LE_{\uparrow}$ (Fig. 19n) and $\Delta H_{\uparrow}$ (Fig. 19m) are also amplified. While $\Delta(R - H_{\uparrow} - LE_{\uparrow})$ is negligible over the land areas, it varies from negative values to positive values over the oceans (Fig. 18c), reflecting presumably the projected changes in heat

exchange between the ocean surface and the atmosphere.

Changes in cloud cover and cloud type affect the radiation fluxes, as was discussed in Chapter 5.3. However, the simulation of clouds is a large source of uncertainty in climate modelling [Boucher et al., 2013] and in simulating the changes in global temperatures [Räisänen, 2016]. We found that the intermodel differences in the projected ΔCLT are large (Fig. 19d), and for the all-sky radiation fluxes the changes in cloud cover contribute to the standard deviations over low-to-mid latitude oceans and the northern high-latitudes. However, the correlation between ΔCLT and ΔT is negligible over many regions, except for parts of the low-to-mid latitude oceans and northern high latitudes (Fig. 21c).

We conclude that even though the turbulent heat fluxes modify the pattern of surface warming, the more interesting factors are the changes in SW and LW fluxes, and the contribution of the water vapor feedback and the snow/ice feedback that alter these radiation fluxes in the climate system (for the all-sky components, the changes in cloud cover are also important). While the strong positive correlation between $\Delta LW_{\downarrow cs}$ and ΔT suggests that a dominating part of the simulated warming is due to enhanced greenhouse effect and changes in the atmospheric re-radiation flux, as anticipated, the strong negative correlation between $\Delta SW_{\downarrow cs}$ and ΔT most likely means that the increase in atmospheric water vapor content also affects the SW radiation fluxes. The contribution of projected increase in absorbed (clear-sky) SW radiation fluxes to current and future global warming could be an interesting aspect for further studies. Donohoe et al. (2014) propose that in the long-term climate simulations, the global warming is driven by enhanced absorption of SW radiation, instead of just the LW radiative forcing by increased greenhouse gases.

As we have noted before, the projections of future climate changes are uncertain due to various reasons, including internal variability in climates system, technical modelling choices and scenario assumptions. By looking at the multimodel projections of the future changes we can characterize plausible outcomes of the future climate system. Additionally, we can get estimates of the uncertainty as well as the model agreement by comparing the consistency of the model-to-model projections using methods described in Chapter 6 or, for further studies, using the methods discussed by Collins and others [Collins et al., 2013]. The confidence in the future projections presented in this thesis could be improved further by adding more climate models to the ensemble or comparing the results from different emission scenarios to RCP8.5.

A weakness in this thesis is that the causes behind the pattern of surface warming cannot be directly deduced with certainty from changes in the energy budget components presented in Chapter 5, even though understanding the effect of feedbacks to the changes in energy fluxes

gives some confidence in the results, and especially the intermodel correlations from Chapter 6.3 give a more straightforward analysis of the plausible relation. One possbile approach is relating ΔT with the energy budget and to express the temperature change in terms of the projected changes in the studied variables, a method suggested for example by Räisänen [Räisänen, 2016]. An advantage of this method is to see more directly the sign and magnitude of the regional temperature change due to each variable, and to compare the dominating factors in different areas. In addition to the geograpical distributions of the changes, changes in the seasonal variation of the energy budget components and their relation to ΔT in different regions could be studied further.

Acknowledgements

I would first like to thank my thesis supervisor Jouni Räisänen for all his guidance and help that he has given me through the process of writing this thesis. I would also like to thank my friends and family for their love, support and encouragement. Finally, I would like to thank all of you who introduced me to the special island of Krakan and its beautiful ocean views. It was a truly inspiring environment to write this thesis. Thank you.

References

[Boucher et al., 2013] Boucher, O., Randall, D., Artaxo, P., Bretherton, C., Feingold, G., Forster, P., Kerminen, V.-M., Kondo, Y., Liao, H., Lohmann, U., Rasch, P., Satheesh, S., Sherwood, S., Stevens, B., and Zhang, X. (2013). "Clouds and Aerosols". *Climate Change 2013: The Physical Science Basis Contribution of Working Group I to the Fifth Assessment Report of the Intergovernmental Panel on Climate Change*. Cambridge University Press.

[Collins et al., 2013] Collins, M., Knutti, R., Arblaster, J., Dufresne, J.-L., Fichefet, T., Friedlingstein, P., Gao, X., Gutowski, W., Johns, T., Krinner, G., Shongwe, M., Tebaldi, C., Weaver, A., and Wehner, M. (2013). "Long-term Climate Change: Projections, Commitments and Irreversibility". *Climate Change 2013: The Physical Science Basis Contribution of Working Group I to the Fifth Assessment Report of the Intergovernmental Panel on Climate Change*. Cambridge University Press.

[Cubasch et al., 2013] Cubasch, U., Wuebbles, D., Chen, D., Facchini, M., Frame, D., Mahowald, N., and Winther, J.-G. (2013). "Introduction". *Climate Change 2013: The Physical Science Basis Contribution of Working Group I to the Fifth Assessment Report of the Intergovernmental Panel on Climate Change*. Cambridge University Press.

[Donohoe et al., 2014] Donohoe, A., Armour, K., Pendergrass, A., and Battisti, D. (2014). "Shortwave and longwave contributions to global warming under increasing CO_2". *PNAS*, 111:16700–16705.

[ENES, 2019a] ENES (2019a). CMIP5 Data Structure. `https://portal.enes.org/data/enes-model-data/cmip5/datastructure`. [Online; accessed 07-September-2019].

[ENES, 2019b] ENES (2019b). CMIP5 Models and Grid Resolution. `https://portal.enes.org/data/enes-model-data/cmip5/resolution`. [Online; accessed 07-September-2019].

[Falloon et al., 2012] Falloon, P., Dankers, R., Betts, R., Jones, C., Booth, B., and Lambert, F. (2012). "Role of vegetation change in future climate under the a1b scenario and a climate stabilisation scenario, using the HadCM3C Earth system model.". *Biogeosciences*, 9:4739–4756.

[Flato et al., 2013] Flato, G., Marotzke, J., Abiodun, B., Braconnot, P., Chou, S., Collins, W., Cox, P., Driouech, F., Emori, S., Eyring, V., Forest, C., Gleckler, P., Guilyardi, E., Jakob, C., Kattsov, V., Reason, C., and Rummukainen, M. (2013). "Evaluation of Climate Models".

Climate Change 2013: The Physical Science Basis Contribution of Working Group I to the Fifth Assessment Report of the Intergovernmental Panel on Climate Change. Cambridge University Press.

[Hansen et al., 2011] Hansen, J., Sato, M., Kharecha, P., and von Schuckmann, K. (2011). "Earth's energy imbalance and implications". *Atmos. Chem. Phys.*, 11:13421–13449.

[Hartmann et al., 2013] Hartmann, D. L., Klein Tank, A., Rusticucci, M., Alexander, L., Brönnimann, S., Charabi, Y., Dentener, F., Dlugokencky, E., Easterling, D., Kaplan, A., Soden, B., Thorne, P., Wild, M., and Zhai, P. (2013). "Observations: Atmosphere and Surface". *Climate Change 2013: The Physical Science Basis Contribution of Working Group I to the Fifth Assessment Report of the Intergovernmental Panel on Climate Change*. Cambridge University Press.

[Holland and Bitz, 2003] Holland, M. and Bitz, C. (2003). "Polar amplification of climate change in coupled models". *Climate Dynamics*, 21:221–232.

[Kiehl and Trenberth, 1997] Kiehl, J. and Trenberth, K. (1997). "Earth's Annual Global Mean Energy Budget". *Bulletin of the American Meteorological Society*, 78:197–208.

[Meehl et al., 2013] Meehl, G., Stocker, T., Collins, W., Friedlingstein, P., Gaye, A., Gregory, J., Kitoh, A., Knutti, R., Murphy, J., Noda, A., Raper, S., Watterson, I., Weaver, A., and Zhao, Z.-C. (2013). "Global climate projections". *Climate Change 2007: The Physical Science Basis. Contribution of Working Group I to the Fourth Assessment Report of the Intergovernmental Panel on Climate Change*. Cambridge University Press.

[Neelin, 2011] Neelin, J. D. (2011). *Climate Change and Climate Modeling*. Cambridge University Press.

[Rhein et al., 2013] Rhein, M., Rintoul, S., Aoki, S., Campos, E., Chambers, D., Feely, R., Gulev, S., Johnson, G., Josey, S., Kostianoy, A., Mauritzen, C., Roemmich, D., Talley, L., and Wang, F. (2013). "Observations: Ocean". *Climate Change 2013: The Physical Science Basis Contribution of Working Group I to the Fifth Assessment Report of the Intergovernmental Panel on Climate Change*. Cambridge University Press.

[Riahi et al., 2011] Riahi, K., Rao, S., Krey, V., Cho, C., Chirkov, V., Fischer, G., Kindermann, G., Nakicenovic, N., and Rafaj, P. (2011). "RCP8.5 – A scenario of comparatively high greenhouse gas emissions". *Climate Change*, 109:33–57.

[Räisänen, 2010] Räisänen, J. (2010). *Fysikaalinen klimatologia*. Helsingin yliopiston fysiikan laitos.

[Räisänen, 2014] Räisänen, J. (2014). *Kasvihuone, ilmastonmuutos ja vaikutukset*. Helsingin yliopiston fysiikan laitos.

[Räisänen, 2016] Räisänen, J. (2016). "An energy balance perspective on regional CO_2-induced temperature changes in CMIP5 models". *Clim. Dyn.*

[Schulzweida, 2019] Schulzweida, U. (2019). CDO User Guide. `https://code.mpimet.mpg.de/projects/cdo/embedded/cdo.pdf`. [Online; version 1.9.6].

[Taylor et al., 2011] Taylor, K., Stouffer, R., and Meehl, G. (2011). "An overview of CMIP5 and the Experiment Design". *Bulletin of the American Meteorological Society*, 93.4:485–498.

[van Vuuren et al., 2011] van Vuuren, D. P., Edmonds, J., Kainuma, M., Riahi, K., Thomson, A., Hibbard, K., Hurtt, G., Kram, T., Krey, V., Lamarque, J.-F., Masui, T., Meinshausen, M., Nakicenovic, N., Smith, S., and Rose, S. (2011). "The representative concentration pathways: an overview". *Climate Change*, 109:5–31.

[Wild et al., 2013] Wild, M., Folini, D., Schär, C., Loeb, N., Dutton, E., and König-Langlo, G. (2013). "The global energy balance from a surface perspective". *Clim. Dyn.*, 40:3107–3134.

[Zhao et al., 1994] Zhao, W., Kuhn, W., and Drayson, S. (1994). "The significance of detailed structure in the boundary layer to thermal radiation at the surface in climate models.". *Geophysical Research Letters*, 21:1631–1634.